UC San Diego
Other Scholarly Work

Title
Combining complementary observing systems to produce a basin-scale network for monitoring upper-ocean transport

Permalink
https://escholarship.org/uc/item/7pg5m20c

Authors
Chandler, Mitchell
Zilberman, Nathalie V.
Sprintall, Janet

Publication Date
2021

Data Availability
The data associated with this publication are within the manuscript.

Combining complementary observing systems to produce a basin-scale network for monitoring upper-ocean transport

Mitchell Chandler[1], Nathalie V. Zilberman, Janet Sprintall

Scripps Institution of Oceanography, La Jolla, CA, USA

January 2021

---

[1] mlchandl@ucsd.edu

Abstract

The high-resolution expendable bathythermograph (HR-XBT) network measures temperature down to approximately 800 m along fixed transects. In comparison, Argo floats are distributed throughout the global ocean and measure temperature and salinity down to approximately 2000 m. Over the 2004-2019 period, the HR-XBT network tended to have a greater sampling density near the coast, while Argo sampling density was generally equivalent to, or greater than, the HR-XBT network in the ocean interior. To take advantage of the benefits of each of these observing systems, a method for combining measurements from HR-XBT, Argo, and satellite altimetry observations was implemented. This method produced estimates of geostrophic velocity and transport in the upper 800 m normal to the HR-XBT transects in the Indian and Pacific Oceans over an approximately 16 year period at high spatial (0.1° along-transect spacing) and temporal (1 month) resolutions. The combined method better resolved the mean geostrophic velocity and transport in the western boundary currents and their recirculations compared to estimates from a 2004-2018 mean high-resolution climatology computed using only Argo data. An additional benefit of the combined method is that it provides a monthly time series of velocity and transport for each HR-XBT transect. This monthly time series captures the temporal variability and will allow for examination of possible drivers of ocean transport.

1. Introduction

The subtropical western boundary currents (WBCs) are strong, poleward-flowing currents located on the western side of the major ocean basins (Fig. 1). They are the largest pathway for the redistribution of oceanic mass and heat from low- to mid-latitudes and therefore play an influential role in the release of heat and moisture to the atmosphere (D. Hu et al., 2015). In turn, this release of heat and moisture can influence weather patterns such as winter storm tracks, and regional climate (D. Hu et al., 2015; Minobe et al., 2008; Nakamura et al., 2008; Njouodo et al., 2018). This transport of heat can also have broader implications on extreme climate variability, for example through marine heatwaves (MHWs) such as the 2015/16 MHW in the Tasman Sea which was caused by anomalously large southward advection of heat in the East Australian Current extension (EACx) (Oliver et al., 2017).

WBCs are expected to change under a warming climate, however it is not clear if all WBCs will demonstrate a consistent trend (D. Hu et al., 2015; S. Hu et al., 2020). For example, Wang et al. (2016) found that the Kuroshio weakened from 1993-2013, despite enhanced warming continuing along its path. Beal and Elipot (2016) found that the Agulhas Current broadened due to increased eddy activity, rather than intensified, over the 1993-2015 period. However, Yang et al. (2016) showed that all WBCs (except the Gulf Stream) are strengthening and shifting poleward. Wu et al. (2012) showed that the WBC regions and their extensions were warming significantly faster than the global mean surface ocean warming rate, which they attributed to a poleward shift (Kuroshio, Gulf Stream, Brazil Current) or intensification (Agulhas Current, EAC, Brazil Current) of the WBCs and their extensions. Using model simulations for the 1990s and 2060s, Oliver and Holbrook (2014) found that transport in the EACx increased, while transport in the Tasman Front (TF) decreased, and transport in the EAC equatorward of the separation point was not significantly changed. These changes were hypothesised as due to an increased [largely unchanged] South Pacific wind stress curl south [north] of the separation point latitude. The simulations also found that sea level variance in the Tasman Sea and EACx increased (possibly due to enhanced eddy activity), and that the EAC separation point shifted poleward (Oliver & Holbrook, 2014). Nonetheless, some of the uncertainty in the response of WBCs may be due to the coarse resolution of climate models, which tend to be poor at resolving the bathymetry, eddies, and other smaller-scale current dynamics of WBC regions (D. Hu et al., 2015). Furthermore, any such trends in these WBCs must be understood on top of the natural and regional variability present in these highly variable systems (D. Hu et al., 2015; Wu et al., 2012; Yang et al., 2016).
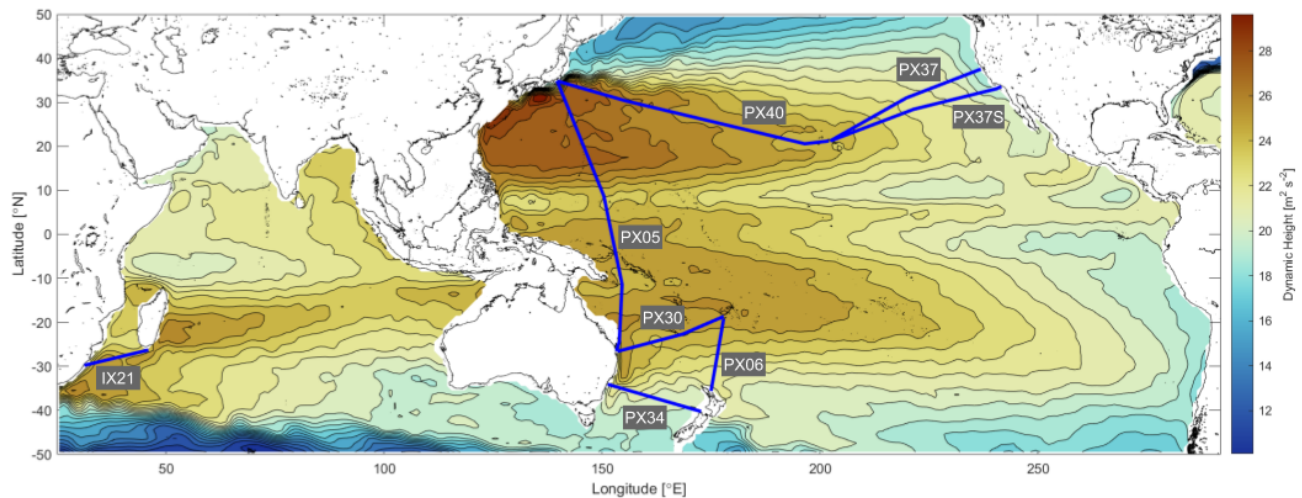
Figure 1: Mean dynamic height (m² s⁻²) at the surface (2.5 dbar) relative to 1975 dbar calculated from the 2004-2018 mean Argo 1°×1° climatology, overlain by the 2004-2019 HR-XBT nominal transects.

Because WBCs are narrow, fast, and highly variable, producing long-term transport estimates based on a single observing system is typically not feasible (Send et al., 2010; Todd et al., 2019). Furthermore, these WBC properties mean that the major broadscale observing systems used in the ocean interior (i.e. Argo and satellite altimetry) tend not to adequately sample WBC regions (Send et al., 2010). Therefore, no single method presently meets all the criteria for sustained observations of transport in both the ocean's boundary currents (BCs) and interior. Because of this, complementary components of the Global Ocean Observing System (GOOS) are sometimes combined to study WBCs (e.g. Beal & Elipot, 2016; Goes et al., 2020; Zilberman et al., 2018). Two components of the GOOS appropriate for such a multi-platform approach are the High-Resolution eXpendable BathyThermograph (HR-XBT) network and the broadscale Argo program. The HR-XBT network (Fig. 1) provides temperature measurements between 0-860 m along fixed transects (Goni et al., 2019). This network collects measurements at spatial and temporal scales that, realistically, cannot presently be reproduced by other existing observing systems over extended time periods (Goni et al., 2019). However, measurements from the HR-XBT network are restricted to these fixed transects, which are only possible where there are stable commercial shipping routes. Furthermore, XBTs only measure temperature over the upper 860 m and therefore lack the salinity profiles required to estimate geostrophic velocities, while also lacking the vertical extent to capture a complete picture of the deep-reaching WBCs (Send et al., 2010). Argo floats are autonomous profiling floats that measure temperature and salinity between roughly 0-2000 m on an approximately 10 day cycle (Riser et al., 2016). The Argo network tends to undersample WBCs, particularly in the near-coastal regions (Riser et al., 2016), and the present distribution of Argo floats is insufficient to sample at the high spatial and

temporal resolutions required to resolve these fast and narrow BCs (Goes et al., 2020; Todd et al., 2019). However, Argo is complementary to the HR-XBT network in that it can be used to measure simultaneous salinity and temperature profiles, produce reference velocity fields (from float trajectories), and provide observations deeper in the water column (Goes et al., 2020; Zilberman et al., 2018). Finally, although neither of these platforms can achieve the high temporal resolution of mooring arrays, the HR-XBT and Argo platforms have the additional benefit of sampling both in the near-coast boundary regions and in the ocean interior (Send et al., 2010).

There is a general consensus that an effective long-term monitoring network is needed to better measure and understand these subtropical WBCs and their interaction with the changing climate (e.g. Beal & Elipot, 2016; D. Hu et al., 2015; Send et al., 2010; Todd et al., 2019; Wu et al., 2012; Yang et al., 2016). The goal of the present study is to make progress towards the development of this long-term monitoring network through the use of complementary elements of the GOOS. To do so, this work builds upon Zilberman et al. (2018) who developed a method to improve long-term volume transport estimates in WBC regions using Argo, HR-XBT, and satellite altimetry. They demonstrated the robustness of the method for the HR-XBT line PX30 between Brisbane, Australia and Suva, Fiji (Fig. 1) through comparisons of their estimates in the EAC with nearby independent moored observations. Specifically, the aims of this study are to 1) combine complementary HR-XBT and Argo data to improve (compared to using solely Argo data) long-term estimates of transport normal to the HR-XBT transects that cross the major BCs and the interior of the Pacific and Indian Oceans, and 2) use these estimates to make recommendations on the sampling density of the HR-XBT program in the Pacific and Indian Oceans. The outline is as follows; the data and methodology is explained in Data and Methods (section 2), followed by comparisons of velocity and transport estimates in Results and Discussion (section 3), and finally the main findings are summarised in Conclusions (section 4). Throughout the report representative figures will be used to highlight key results. Figures for all transects are included in the Appendices.

2. Data and Methods

2.1. Data

Data from three different observing systems were used; HR-XBT, Argo, and satellite altimetry. HR-XBT transects are occupied nominally four times a year with temperature measured down to roughly 860 m at approximately 10-50 km intervals along each transect (Goni et al., 2019). Some HR-XBT transects have been occupied for more than 30 years, though, to coincide with the Argo period, only transects between 2004-2019 were considered here. For each transect, temperature was objectively mapped onto 10 m depth intervals from 0-800 m, and 0.1° intervals in longitude [latitude] for the zonal [meridional] transects. Corresponding salinity data for each HR-XBT transect was obtained using temperature-salinity relationships based on Argo data, following the method described in Zilberman et al. (2018). The resulting salinity product has the same resolution as the gridded HR-XBT temperature dataset (0.1° longitude grid for zonal transects or 0.1° latitude grid for meridional transects, and 10 m depth intervals from 0-800 m).

Argo temperature and salinity data were from the high-resolution gridded 1/6°×1/6° 2004-2018 mean Roemmich-Gilson Argo temperature and salinity climatologies (Roemmich & Gilson, 2009). The climatologies were constructed using a weighted least squares fit of the nearest 33 profiles per month, with the data on 58 standard pressure levels. The 2004-2018 mean is not significantly different from the 2004-2019 mean, though future work will use an updated mean Argo climatology.

The satellite altimetry data was the "Global Ocean Gridded L4 Sea Surface Heights and Derived Variables Reprocessed (1993-ongoing)" dataset from the EU Copernicus Marine Service. This dataset has both daily-mean sea level anomaly (SLA) and monthly-mean SLA referenced to the 1993-2012 period on a 1/4°×1/4° grid. Both daily-mean and monthly-mean SLAs were considered from 2004 through to the end of each dataset (15th October 2019 for the daily-mean, September 2019 for the monthly-mean).

2.2. Construction of HR-XBT Nominal Transects

Nominal transects were produced for each of the HR-XBT lines (Fig. 1) using transects from the 2004-2019 period (Table 1). Outlier transects (such as those which visited a port away from the most commonly occupied route) were removed and the remaining transects averaged in time. This time-averaged transect was linearised to obtain the nominal transect. Some transects were best represented by a single straight-line segment (e.g. PX34), while for others the nominal transect was

7

best represented by a series of connected straight-line segments (e.g. PX30). The ends of transects where the line changed directions towards a port were also excluded (e.g. PX30 into Suva, Fiji; PX40 past Bōsō Peninsula toward Yokohama, Japan; PX37 and PX37S into Honolulu, USA; and PX06 into Suva, Fiji).

Table 1: Earliest and latest timestamps of the HR-XBT transects, the number of transects in the time period, and the maximum number of days needed to complete a transect for the 2004-2019 period.

HR-XBT line	Start Date	End Date	Number of Transects	Days to Complete
IX21	26-Mar-2004	05-Nov-2019	58	9
PX05	16-Aug-2009	12-Jul-2019	40	13
PX06	09-Apr-2004	16-Dec-2019	73	5
PX30	02-Jan-2004	25-Oct-2019	56	8
PX34	02-Jan-2004	01-Dec-2019	60	6
PX37	08-Jan-2004	12-Oct-2019	55	6
PX37S	15-Nov-2008	05-Oct-2019	53	6
PX40	10-Nov-2012	01-Nov-2019	30	15

2.3. Comparing Argo and HR-XBT Profiling Density

To demonstrate the complementarity of the HR-XBT and Argo networks, the sampling of each observing system around the nominal transects was compared. For this comparison, the raw HR-XBT and Argo profiles for the 2004-2019 period were binned into 0.5° along-transect × 3° across-transect orthogonal bins centred on the nominal transects. All Argo and HR-XBT profiles were considered in the binning procedure, including those HR-XBT transects which were considered as outliers for determining the nominal transect. The location and time at the end of each Argo cycle was used for the analysis. For transects consisting of multiple straight line segments, the rectangular bins were connected where the transect changed direction so that there were no gaps between bins.

The HR-XBT and Argo sampling distributions along two representative transects (Fig. 2) clearly shows the complementarity of the observing systems. The number of HR-XBT profiles is significantly higher in the coastal regions, including the WBC systems, while the number of Argo profiles tends to be

similar to, or even greater than, the number of HR-XBT profiles in the interior. The number of Argo profiles is particularly high in the interior of PX40 (right panel), and these regions near Japan and Hawaii are known to have a high Argo sampling density (e.g. Davis et al., 2019). In comparison, for PX30 (Fig. A8) there tend to be more HR-XBT profiles in the interior than Argo profiles. There are a number of island chains and regions of bathymetry shallower than the Argo float nominal parking depth of 1000 m near PX30, which likely results in a reduced number of Argo profiles. For all the transects, higher numbers of Argo float deployments are often responsible for an elevated number of Argo profiles in specific years (e.g. IX21 in 2013, and PX40 near Japan in 2004-2006).
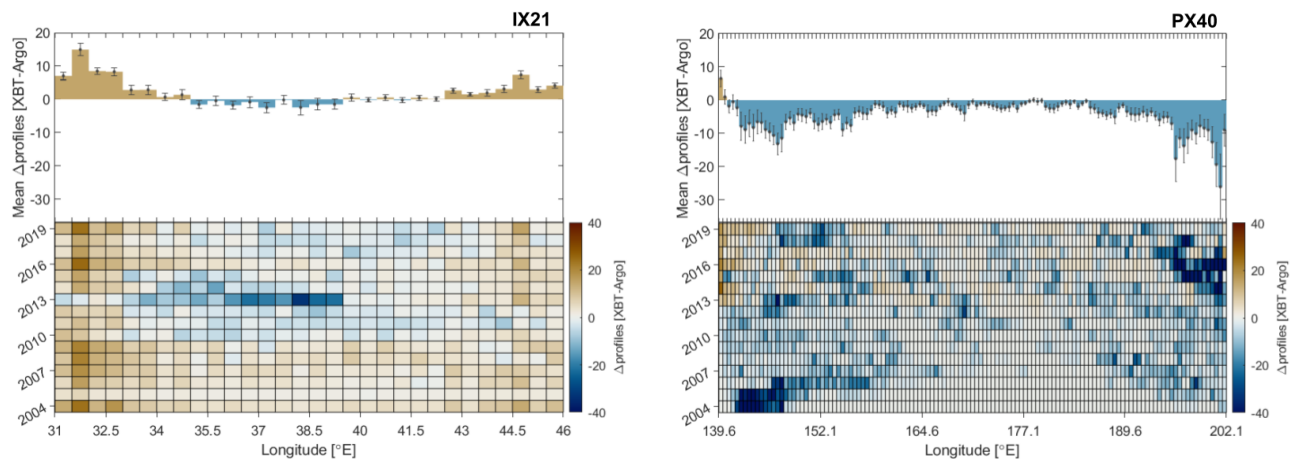
Figure 2: Difference in the number of HR-XBT and Argo profiles for 2004-2019 in each 0.5°×3° orthogonal bin around *(left)* IX21 and *(right)* PX40. Positive values (brown colours) indicate more HR-XBT profiles than Argo profiles. The histograms give the 2004-2019 yearly-averaged difference in the number of profiles, and the heatmaps give the difference in the number of profiles for each individual year. Error bars on the histograms represent ±1 standard error. For the heatmaps the colour range is restricted to ±40 so some cells are saturated.

2.4. Combining HR-XBT and Argo

Because individual occupations of each HR-XBT transect do not follow the exact same route, temperature and salinity measurements from each individual transect were projected onto the nominal transect using the Argo mean temperature and salinity climatologies. The individual transects (Fig. 3) were linearised in along-track distance coordinates and the angle of rotation relative to the nominal transect calculated. This angle was used to find the distances along each transect perpendicular to the positions on the nominal transect. HR-XBT temperature and salinity were then linearly interpolated onto these new distance coordinates (perpendicular to the nominal transect) for each individual transect.

To extend the Argo climatology coverage near the coasts, temperature and salinity were repeated by one grid point. Argo temperature and salinity were then linearly interpolated onto the positions of each individual HR-XBT transect perpendicular to the nominal transect and onto the HR-XBT 10 m depth levels. The difference between the Argo temperature and salinity along an individual transect and the Argo temperature and salinity along the nominal transect was added to the HR-XBT temperature and salinity to produce an adjusted temperature and salinity on the nominal transect. For transects that had multiple linear segments, this method was applied to each segment. Finally, the transect end points were chosen to coincide with where the majority of the individual transects ended, so that estimates at the ends of the nominal transect were not disproportionately influenced by just a few transects. Estimates from this method are referred to in the following as HR-XBT+Argo.
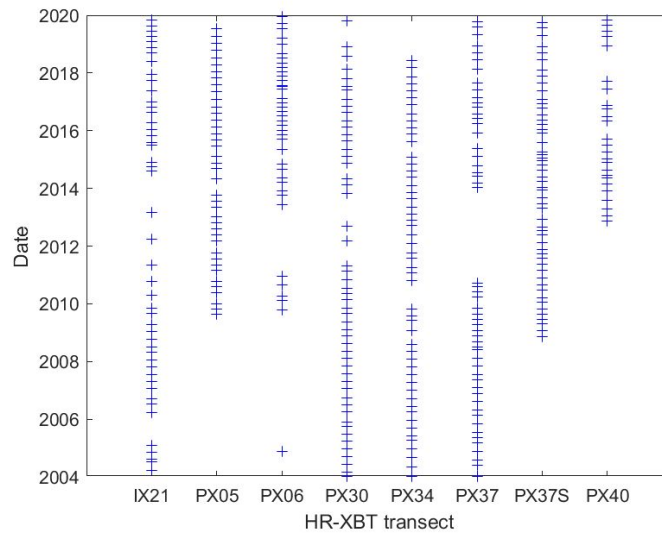
Figure 3: Dates of the transects used in the HR-XBT+Argo combined method for each of the HR-XBT transects (IX21, PX05, PX06, PX30, PX34, PX37, PX37S, and PX40).

2.5. Combining Satellite Altimetry with HR-XBT and Argo

Because HR-XBT sampling is repeated along each transect on a nominally quarterly basis, satellite altimetry was combined with the HR-XBT+Argo data through a regression relationship between the altimetric SLA and steric height (h) at the time of each HR-XBT transect. This regression allowed for monthly estimates of h, resulting in increased temporal resolution. To implement this, SLAs were interpolated onto each nominal transect and the time-mean was removed to find the SLA temporal anomaly (SLA') for both the daily-mean and monthly-mean SLA products. For each individual HR-XBT transect, the daily-mean SLA' was averaged over the maximum number of days it took to complete a transect (Table 1) as individual transects were considered to be representative of the synoptic

conditions. HR-XBT+Argo temperature and salinity were used to calculate h relative to 800 m ($h(z/800)$). The time-mean h at each coordinate (x) and depth (z) was removed to obtain the h temporal anomaly (h'). A linear regression was calculated between h' and the multi-day averaged SLA' at each coordinate and depth along the nominal transect.

$$h'(z/800)(x) \approx m(x,z) \times SLA'(x) + c(x,z) \qquad (1)$$

where m and c are the gradient and intercept regression coefficients respectively. Equation (1) was applied to each monthly-mean SLA' to obtain monthly estimates of h'. The time-mean h was added back in and the monthly h was converted to dynamic height (H) by multiplying by gravity (g = 9.81 m s^{-2}). Estimates from this method are referred to in the following as HR-XBT+Argo+Altimetry.

2.6. Calculating Geostrophic Velocity and Transport

To compute geostrophic velocities normal to each of the nominal HR-XBT transects, H was calculated relative to the shallower of either the ETOPO2 bathymetry (Smith & Sandwell, 1997) or 800 m. Geostrophic velocity (v_g, u_g) normal to each transect was then calculated relative to a level of no motion (LNM) from the thermal wind relation (e.g. Gill, 1982).

$$v_g(p) = \frac{1}{f}\frac{\partial}{\partial x}[H(p) - H(p_0)]$$

$$u_g(p) = \frac{-1}{f}\frac{\partial}{\partial y}[H(p) - H(p_0)]$$

where p is a given pressure level, p_0 is the pressure at the LNM, and f is the Coriolis parameter. For each location along the transect, the LNM (p_0) was taken to be 800 m, or the bathymetry if shallower. Centred differencing was used to calculate the spatial derivatives, with H repeated as ghost points at the ends of the transects.

Geostrophic transport was determined as the depth-integrated geostrophic velocity multiplied by the distance between measurements along the transect. Transport values were cumulatively summed along-transect using a midpoint Riemann sum to obtain the eastward-accumulated [northward-accumulated] transport along each zonal [meridional] nominal transect.

For both HR-XBT+Argo and HR-XBT+Argo+Altimetry, geostrophic velocity and transport were time-averaged over the length of the respective record to obtain the mean geostrophic velocity and mean transport.

Finally, for comparison with the HR-XBT+Argo and HR-XBT+Argo+Altimetry estimates, the high-resolution 2004-2018 mean Argo temperature and salinity climatologies were linearly interpolated

onto each nominal transect and onto the same depth levels as the HR-XBT data to construct Argo-only estimates of the mean geostrophic velocity and transport.

3. Results and Discussion

Estimates of geostrophic velocity and accumulated transport in the upper 800 m computed using each of the Argo-only, HR-XBT+Argo, and HR-XBT+Argo+Altimetry data sets were compared for each HR-XBT transect.

The mean depth-integrated (0-800 m) velocities from the HR-XBT+Argo+Altimetry method are presented in Fig. 4 for the transects that sample WBC regions. It is clear that the subtropical WBCs (EAC, Kuroshio, Agulhas Current), which are visible as the strong poleward flows on the western boundaries of the ocean basins, are all resolved by the combined method. In the case of the Kuroshio and EAC, clear recirculations are also evident as the relatively strong equatorward flows immediately to the east of the poleward WBC flows. The predominantly eastward flows associated with the bifurcation of the EAC south of 30°S (Ridgway & Dunn, 2003) are evident between New Zealand and Fiji. Reversals in the flow direction along a transect are likely due to the presence of eddies.
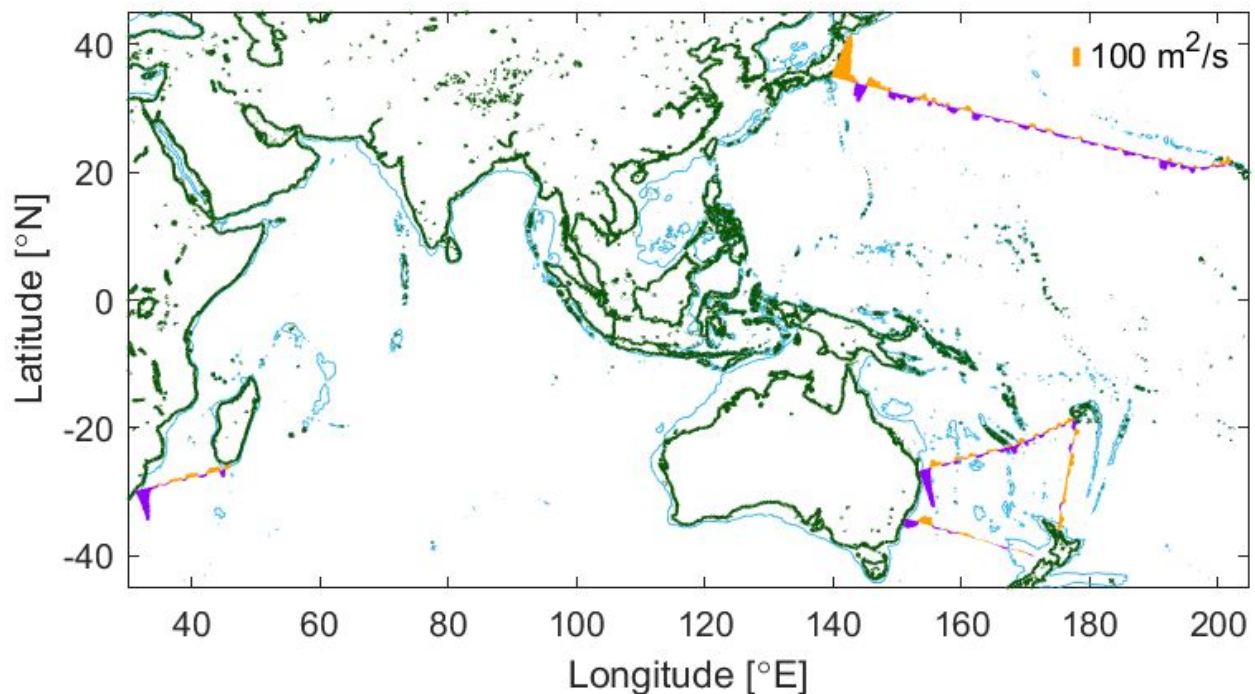
Figure 4: HR-XBT+Argo+Altimetry 2004-2019 mean depth-integrated (0-800 m) velocity normal to each of the nominal transects. Eastward or northward [westward or southward] depth-integrated velocities are coloured orange [purple] and the length of each bar is proportional to the magnitude of the depth-integrated velocity. A 100 m^2 s^{-1} reference bar is included in the top right. Contours indicate the coastline (green) and a depth of 1000 m (light blue).

Examples of the mean geostrophic velocity estimate using Argo-only and using HR-XBT+Argo+Altimetry are considered for IX21 in the western Indian Ocean (Fig. 5). This transect samples the Agulhas Current, which is evident in both velocity sections as the strong southward (i.e. negative) velocities at the western edge of the transect. It is clear that the HR-XBT+Argo+Altimetry method (right panel) better resolves the structure of the WBC compared to the Argo-only method (left panel) as the velocities are stronger in the core of the current and the core is better defined. In comparison, the Agulhas Current velocities are smeared out and weaker in the Argo-only estimate. At this western edge, the use of HR-XBT measurements enables the HR-XBT+Argo+Altimetry cross-section to extend closer to the African coast compared to the Argo-only estimate. This difference in extent is due to the shallower bathymetry near the South African coast which results in reduced Argo sampling (Fig. 2). At the eastern end of the transect, HR-XBT+Argo+Altimetry shows stronger northward velocities compared to the weak southward velocities in the Argo-only estimate. This region off southern Madagascar is known to be highly variable (e.g. T. Morris et al., 2019; Ridderinkhof et al., 2013), which is evident in the variability from transect to transect (not shown, but see also Fig. A31). Additionally, both Argo and altimetry measurements at this eastern edge may be influenced by the proximity of the nominal transect to the shallow bathymetry around southern Madagascar.
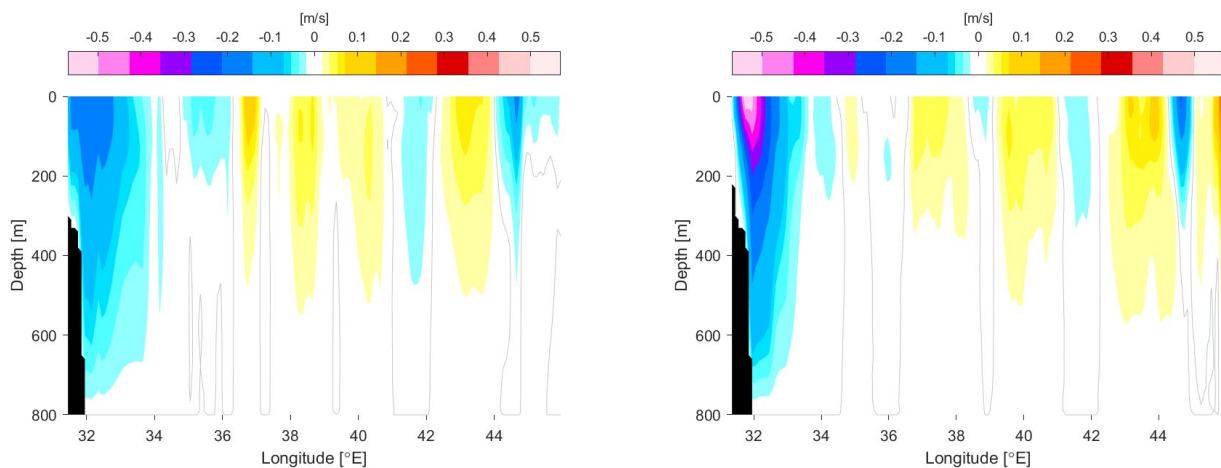
Figure 5: Mean geostrophic velocity relative to 800 m normal to the IX21 nominal transect for *(left)* Argo-only 2004-2018 climatology, and *(right)* HR-XBT+Argo+Altimetry averaged between January 2004-September 2019. Negative [positive] velocities are southward [northward] and the zero velocity contour is indicated in grey.

Similar to IX21, the mean velocity cross-sections for the other HR-XBT transects also show clearly evident WBCs. In particular, PX30 and PX40, which cross the EAC and Kuroshio respectively, have stronger and more defined WBC jets in the HR-XBT+Argo+Altimetry section (Fig. A11 and A21) compared to the Argo-only section (Fig. A9 and A23). PX34 and PX06, crossing the EACx and EAuC

respectively, have an almost double jet feature in their BC regions (Fig. A17 and A5). The corresponding depth-integrated velocity time series (Fig. A19 and A7) suggest that these double jet features are due to variability in the location of the WBC.

Two examples of the eastward-accumulated transport estimates for each of the three methods are examined for the EAC/Tasman Sea region (Fig. 6). The first of these (PX30, left panel) samples the EAC, and it can be seen that both the HR-XBT+Argo and HR-XBT+Argo+Altimetry methods resolve similar strength EACs which are stronger than that estimated from the Argo-only method. The second (PX34, right panel) samples the EACx and here the HR-XBT+Argo and HR-XBT+Argo+Altimetry methods resolve a much stronger and clearer recirculation, though all three methods resolve a similar strength poleward EACx. In general, differences in the estimated WBC and/or recirculation transport can significantly impact the estimate of total transport across a section, even if the patterns of accumulated transport are similar in the interior. Examining the interior transport, for PX30 there is more point-to-point variability along the transect in both the HR-XBT+Argo and HR-XBT+Argo+Altimetry methods compared to the smoother Argo-only curve due to the higher spatial sampling resolution afforded by HR-XBTs. There is also a difference in the Argo-only estimate at the eastern edge of PX34, and this is likely due to the bathymetry in this region being shallower than the 1000 m Argo float nominal parking depth which results in there being fewer Argo profiles (Fig. A14).
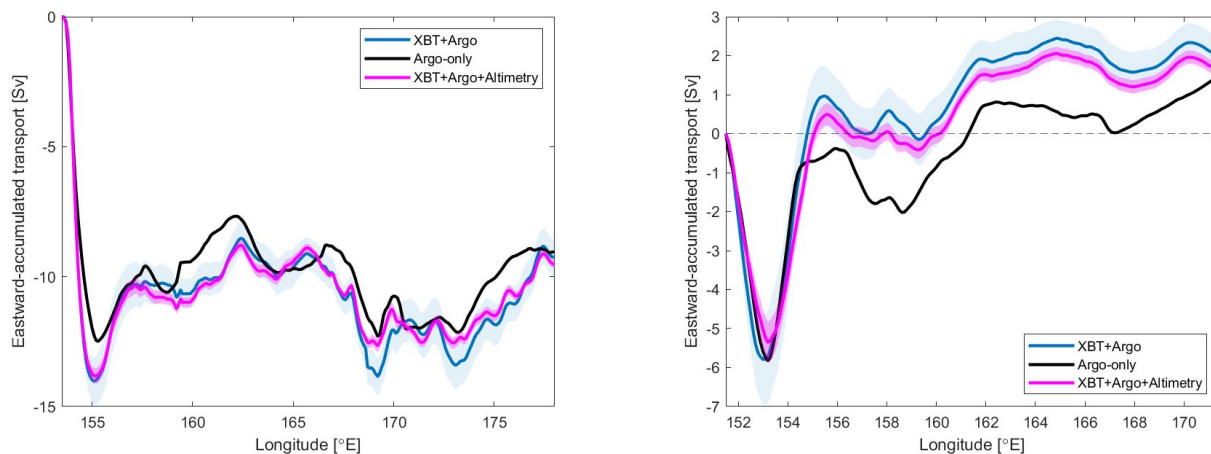
Figure 6: Mean eastward-accumulated geostrophic transport (Sv) relative to 800 m normal to the *(left)* PX30 and *(right)* PX34 nominal transects for HR-XBT+Argo (2004-2019 mean, blue), HR-XBT+Argo+Altimetry (2004-September 2019 mean, pink), and Argo-only (2004-2018 mean, black). The shading indicates ±1 standard error. Negative [positive] transports are southward [northward].

A better resolved WBC system (i.e. stronger poleward flowing WBC and/or stronger equatorward flowing recirculation) using the HR-XBT+Argo+Altimetry method and similar interior patterns between all three methods were also found for other HR-XBT transects. However, some other features were unique to specific transects. For example, the HR-XBT+Argo and HR-XBT+Argo+Altimetry methods identify an eastward jet at roughly 20-21°S along PX06 that is not seen in the Argo-only method (Fig. A6). Using HR-XBT data, M. Morris et al. (1996) also found a filament of eastward geostrophic flow along this same transect at approximately 21°S. This jet therefore seems to be a robust feature of the regional oceanography that is not being resolved by the Argo-only estimate.

It is also worth noting that, unsurprisingly, the HR-XBT+Argo and HR-XBT+Argo+Altimetry transport estimates tend to be more similar when there are more HR-XBT transects distributed throughout the 2004-2019 period, as is the case for PX30 and PX34 which both have over 50 transects since 2004 (Table 1). In comparison, PX40 only has 30 total transects beginning in November 2012 (Table 1), and has larger differences between the HR-XBT+Argo and HR-XBT+Argo+Altimetry transport estimates in the Kuroshio region (Fig. A24, left panel). However, if HR-XBT+Argo+Altimetry along PX40 is averaged over the same time period as the PX40 HR-XBT transects (i.e. from November 2012 onward), then the HR-XBT+Argo and HR-XBT+Argo+Altimetry mean transport estimates are more similar (Fig. A24, right panel). In particular, the HR-XBT+Argo+Altimetry recirculation is weaker when considering the November 2012-September 2019 period compared to the 2004-September 2019 period. This result suggests high temporal variability in the Kuroshio system, and also points towards the ability of a longer time series to more accurately represent the true mean and variability.

Finally, an example monthly time series of the depth-integrated geostrophic velocity computed using the HR-XBT+Argo+Altimetry dataset is considered for PX40 between Japan and Hawaii (Fig. 7). The black arrows on the right side of the figure are the dates of each individual HR-XBT transect. Clearly the irregular HR-XBT transects alone are insufficient to produce a regular monthly time series. The monthly time series is therefore only possible when altimetry data is included as well. Furthermore, for this particular transect, there are only HR-XBT transects from November 2012 onward. Therefore the use of altimetry allows for the full 2004-2019 record to be determined. The strong northward depth-integrated velocities at the western end of the transect are indicative of the Kuroshio, and variability in both the strength and width of this WBC can clearly be seen. The recirculation is evident as the relatively strong southward depth-integrated velocities just to the east of the poleward WBC flow, and there is significant variability in this recirculation as well. For example, the recirculation appears to be stronger during the 2005-2010 period. The Kuroshio Extension is known to alternate

between more and less vigorous meandering states on decadal time scales (Qiu & Chen, 2005). Jayne et al. (2009) captured a change in the meandering regime from weakly to strongly meandering in late 2004, which seems to coincide with the occurrence of the stronger southward depth-integrated velocities seen here in the recirculation. The time series also captures westward propagating features (e.g. Rossby waves). Clearly there are a number of interesting features, and future analyses will examine this variability and the mechanisms that drive it.
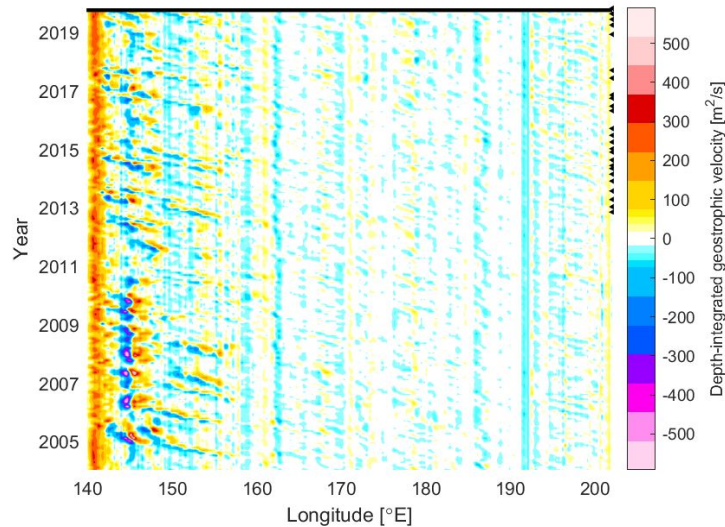
Figure 7: Monthly depth-integrated (0-800 m) geostrophic velocity (m^2 s^{-1}) normal to PX40 from HR-XBT+Argo+Altimetry. Positive [negative] velocities are northward [southward]. The black arrows on the right indicate the times of the HR-XBT transects.

The obvious but variable WBC system in PX40 is representative of the WBC systems shown in the depth-integrated velocity hovmöllers for the other transects. However, an extreme example of WBC variability can be seen along PX34 (Fig. A19). Although there is a general poleward flowing EACx and equatorward flowing recirculation evident, the flow is not coherent in time. Rather, the poleward flow in the EACx tends to occur in a series of eddies (e.g. Oke et al., 2019).

4. Conclusions

The aim of this study was to combine HR-XBT and Argo measurements to obtain long-term high-resolution estimates of transport across the HR-XBT transects of the Pacific and Indian Oceans, with the additional goal of using these estimates to guide recommendations on the HR-XBT program. It has been shown that HR-XBT sampling density tends to be greater near the coasts (particularly in the BC regions), while Argo sampling density is generally adequate in the interior. The Argo network can therefore resolve the weaker interior flows, but struggles to adequately resolve the WBC regions. In comparison, the higher HR-XBT sampling density means that the combined method tends to better resolve velocity and transport in the WBCs and their recirculations. Furthermore, because HR-XBTs sample both close to the coast and into the ocean interior, the estimates from the combined method are able to capture meandering of the current in the transition zone between the near-coast WBC and the interior. Capturing the full offshore extent of the WBC systems will allow for calculations of the net transport in these systems. The long running records of some of these HR-XBT transects are also important for enabling longer-term estimates of velocity and transport. Additionally, the inclusion of satellite altimetry means that monthly estimates of velocity and transport can be produced, better resolving the temporal variability, which will allow for comparisons of transport variability with possible drivers.

The key benefit of combining measurements from the HR-XBT, Argo, and satellite altimetry observing networks is that estimates of geostrophic velocity and transport in the upper 800 m can be obtained at relatively high temporal (1 month) and spatial (0.1° along-transect spacing) resolutions over an approximately 16 year period. At present, no single observing system can realistically produce estimates of WBC variability at similar resolutions over a similar period. However, this technique comes with some caveats. For example, because both HR-XBT measurements and the Argo climatology are required, in cases where the HR-XBT measurements extend closer to the coast than the Argo climatology some measurements are unable to be included. This could lead to estimates missing the inshore signature of currents on the continental shelf. In addition, estimates could be biased if HR-XBT transects predominantly occur during a particular time of the year or are more often during some years, rather than measurements being spaced throughout the year and over the full time period considered. To combat this, it is important to ensure that HR-XBT transects continue to be regularly repeated throughout the year. Because of the multi-decadal HR-XBT time series, for the most part at least one transect from each calendar month was available for all of the nominal transects. The exceptions to this were PX40 (no transects from March were used) and PX05 (no

transects from December), where HR-XBT transects only began in November 2012 and August 2009 respectively.

Additionally, this work demonstrates the limitations in Argo sampling near the coasts and in particular in the WBC regions. The lack of floats in coastal regions is a by-product of the 1000 m nominal Argo float parking depth, while Argo undersampling in WBC regions is a known limitation due to the swift WBC flows. As such, the Argo program plans to double the number of floats in these WBC regions (Roemmich et al., 2019).

In the future, autonomous underwater glider networks have the potential for providing high spatial resolution measurements within WBC systems year-round. Glider measurements have been sporadically undertaken to varying extents in a number of subtropical BC systems including the Agulhas Current, California Current, EAC, Gulf Stream, and Kuroshio (see Todd et al., 2019 and references therein). Future work may consider how complementary glider measurements could be incorporated to further improve estimates of upper-ocean transport in BC regions and the ocean's interior.

Acknowledgements

References

Beal, L. M., & Elipot, S. (2016). Broadening not strengthening of the Agulhas Current since the early 1990s. *Nature*, *540*(7634), 570–573. https://doi.org/10.1038/nature19853

Davis, R. E., Talley, L. D., Roemmich, D., Owens, W. B., Rudnick, D. L., Toole, J., et al. (2019). 100 Years of Progress in Ocean Observing Systems. *Meteorological Monographs*, *59*, 3.1-3.46. https://doi.org/10.1175/AMSMONOGRAPHS-D-18-0014.1

Gill, A. E. (1982). *Atmosphere-Ocean Dynamics*. Academic Press.

Goes, M., Goni, G., Dong, S., Boyer, T., & Baringer, M. (2020). The complementary value of XBT and Argo observations to monitor ocean boundary currents and meridional heat and volume transports: A case study in the Atlantic Ocean. *Journal of Atmospheric and Oceanic Technology*, 1–42. https://doi.org/10.1175/JTECH-D-20-0027.1

Goni, G. J., Sprintall, J., Bringas, F., Cheng, L., Cirano, M., Dong, S., et al. (2019). More Than 50 Years of Successful Continuous Temperature Section Measurements by the Global Expendable Bathythermograph Network, Its Integrability, Societal Benefits, and Future. *Frontiers in Marine Science*, *6*. https://doi.org/10.3389/fmars.2019.00452

Hu, D., Wu, L., Cai, W., Gupta, A. S., Ganachaud, A., Qiu, B., et al. (2015). Pacific western boundary currents and their roles in climate. *Nature*, *522*(7556), 299–308. https://doi.org/10.1038/nature14504

Hu, S., Sprintall, J., Guan, C., McPhaden, M. J., Wang, F., Hu, D., & Cai, W. (2020). Deep-reaching acceleration of global mean ocean circulation over the past two decades. *Science Advances*, *6*(6), eaax7727. https://doi.org/10.1126/sciadv.aax7727

Jayne, S. R., Hogg, N. G., Waterman, S. N., Rainville, L., Donohue, K. A., Randolph Watts, D., et al. (2009). The Kuroshio Extension and its recirculation gyres. *Deep Sea Research Part I: Oceanographic Research Papers*, *56*(12), 2088–2099. https://doi.org/10.1016/j.dsr.2009.08.006

Minobe, S., Kuwano-Yoshida, A., Komori, N., Xie, S.-P., & Small, R. J. (2008). Influence of the Gulf

      Stream on the troposphere. *Nature*, *452*(7184), 206–209. https://doi.org/10.1038/nature06690

Morris, M., Roemmich, D., & Cornuelle, B. (1996). Observations of Variability in the South Pacific

      Subtropical Gyre. *Journal of Physical Oceanography*, *26*(11), 2359–2380.

      https://doi.org/10.1175/1520-0485(1996)026<2359:OOVITS>2.0.CO;2

Morris, T., Aguiar-González, B., Ansorge, I., & Hermes, J. (2019). Lagrangian Evolution of Two

      Madagascar Cyclonic Eddies: Geometric Properties, Vertical Structure, and Fluxes. *Journal of*

      Geophysical Research: Oceans, *124*(11), 8193–8218. https://doi.org/10.1029/2019JC015090

Nakamura, H., Sampe, T., Goto, A., Ohfuchi, W., & Xie, S.-P. (2008). On the importance of midlatitude

      oceanic frontal zones for the mean state and dominant variability in the tropospheric

      circulation. *Geophysical Research Letters*, *35*(15). https://doi.org/10.1029/2008GL034010

Njouodo, A. S. N., Koseki, S., Keenlyside, N., & Rouault, M. (2018). Atmospheric Signature of the

      Agulhas Current. *Geophysical Research Letters*, *45*(10), 5185–5193.

      https://doi.org/10.1029/2018GL077042

Oke, P. R., Roughan, M., Cetina-Heredia, P., Pilo, G. S., Ridgway, K. R., Rykova, T., et al. (2019).

      Revisiting the circulation of the East Australian Current: Its path, separation, and eddy field.

      Progress in Oceanography, *176*, 102139. https://doi.org/10.1016/j.pocean.2019.102139

Oliver, E. C. J., & Holbrook, N. J. (2014). Extending our understanding of South Pacific gyre "spin-up":

      Modeling the East Australian Current in a future climate. *Journal of Geophysical Research:*

      Oceans, *119*(5), 2788–2805. https://doi.org/10.1002/2013JC009591

Oliver, E. C. J., Benthuysen, J. A., Bindoff, N. L., Hobday, A. J., Holbrook, N. J., Mundy, C. N., &

      Perkins-Kirkpatrick, S. E. (2017). The unprecedented 2015/16 Tasman Sea marine heatwave.

      Nature Communications, *8*(1), 16101. https://doi.org/10.1038/ncomms16101

Qiu, B., & Chen, S. (2005). Variability of the Kuroshio Extension Jet, Recirculation Gyre, and

      Mesoscale Eddies on Decadal Time Scales. *Journal of Physical Oceanography*, *35*(11),

2090–2103. https://doi.org/10.1175/JPO2807.1

Ridderinkhof, W., Bars, D. L., Heydt, A. S. von der, & Ruijter, W. P. M. de. (2013). Dipoles of the South
East Madagascar Current. *Geophysical Research Letters*, *40*(3), 558–562.
https://doi.org/10.1002/grl.50157

Ridgway, K. R., & Dunn, J. R. (2003). Mesoscale structure of the mean East Australian Current
System and its relationship with topography. *Progress in Oceanography*, *56*(2), 189–222.
https://doi.org/10.1016/S0079-6611(03)00004-1

Riser, S. C., Freeland, H. J., Roemmich, D., Wijffels, S., Troisi, A., Belbéoch, M., et al. (2016). Fifteen
years of ocean observations with the global Argo array. *Nature Climate Change*, *6*(2),
145–153. https://doi.org/10.1038/nclimate2872

Roemmich, D., & Gilson, J. (2009). The 2004–2008 mean and annual cycle of temperature, salinity,
and steric height in the global ocean from the Argo Program. *Progress in Oceanography*, *82*(2),
81–100. https://doi.org/10.1016/j.pocean.2009.03.004

Roemmich, D., Alford, M. H., Claustre, H., Johnson, K., King, B., Moum, J., et al. (2019). On the
Future of Argo: A Global, Full-Depth, Multi-Disciplinary Array. *Frontiers in Marine Science*, *6*.
https://doi.org/10.3389/fmars.2019.00439

Send, U., Davis, R., Fischer, J., Imawaki, S., Kessler, W., Meinen, C., et al. (2010). A Global Boundary
Current Circulation Observing Network. In *Proceedings of OceanObs'09: Sustained Ocean
Observations and Information for Society* (Vol. 2). Venice, Italy: European Space Agency.
https://doi.org/10.5270/OceanObs09.cwp.78

Smith, W. H. F., & Sandwell, D. T. (1997). Global Sea Floor Topography from Satellite Altimetry and
Ship Depth Soundings. *Science*, *277*(5334), 1956–1962.
https://doi.org/10.1126/science.277.5334.1956

Todd, R. E., Chavez, F. P., Clayton, S., Cravatte, S., Goes, M., Graco, M., et al. (2019). Global
Perspectives on Observing Ocean Boundary Current Systems. *Frontiers in Marine Science*, *6*.

https://doi.org/10.3389/fmars.2019.00423

Wang, Y.-L., Wu, C.-R., & Chao, S.-Y. (2016). Warming and weakening trends of the Kuroshio during

1993–2013. *Geophysical Research Letters*, *43*(17), 9200–9207.

https://doi.org/10.1002/2016GL069432

Wu, L., Cai, W., Zhang, L., Nakamura, H., Timmermann, A., Joyce, T., et al. (2012). Enhanced

warming over the global subtropical western boundary currents. *Nature Climate Change*, *2*(3),

161–166. https://doi.org/10.1038/nclimate1353

Yang, H., Lohmann, G., Wei, W., Dima, M., Ionita, M., & Liu, J. (2016). Intensification and poleward

shift of subtropical western boundary currents in a warming climate. *Journal of Geophysical

Research: Oceans*, *121*(7), 4928–4945. https://doi.org/10.1002/2015JC011513

Zilberman, N. V., Roemmich, D. H., Gille, S. T., & Gilson, J. (2018). Estimating the Velocity and

Transport of Western Boundary Current Systems: A Case Study of the East Australian Current

near Brisbane. *Journal of Atmospheric and Oceanic Technology*, *35*(6), 1313–1329.

https://doi.org/10.1175/JTECH-D-17-0153.1

Appendices
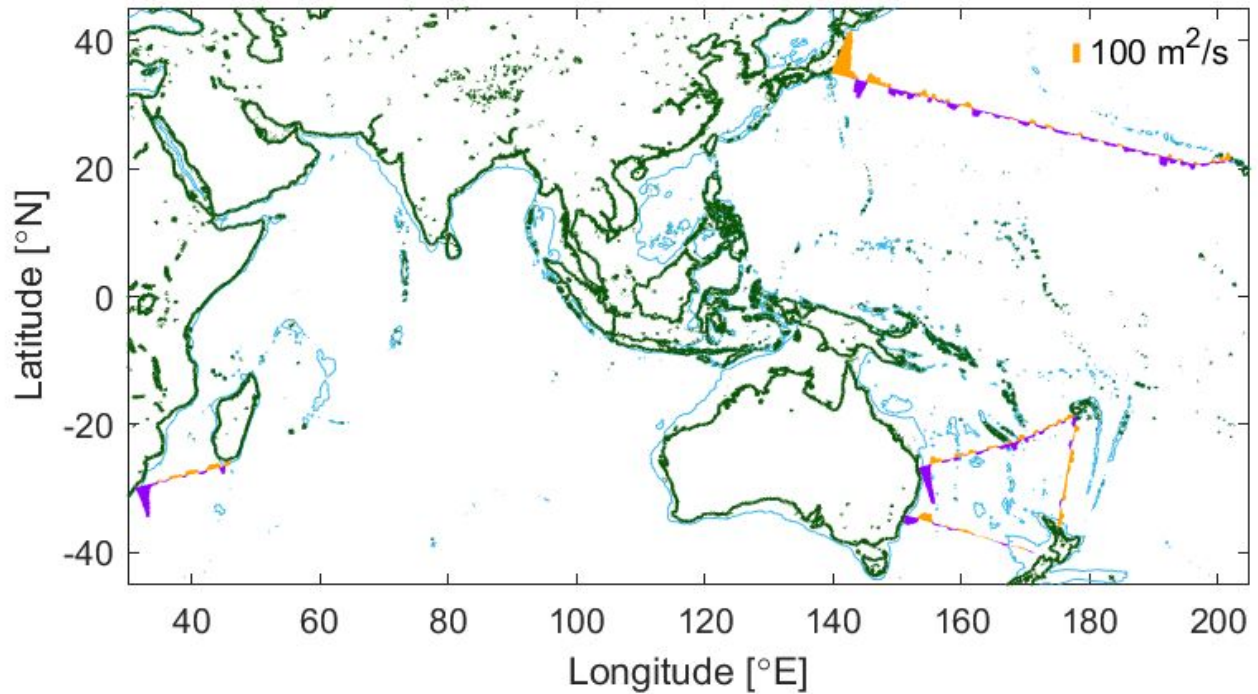
Figure A1: HR-XBT+Argo+Altimetry 2004-2019 mean depth-integrated (0-800 m) velocity normal to each of the nominal transects. Eastward or northward [westward or southward] depth-integrated velocities are coloured orange [purple] and the length of each bar is proportional to the magnitude of the depth-integrated velocity. A 100 m^2 s^{-1} reference bar is included in the top right. Contours indicate the coastline (green) and a depth of 1000 m (light blue).
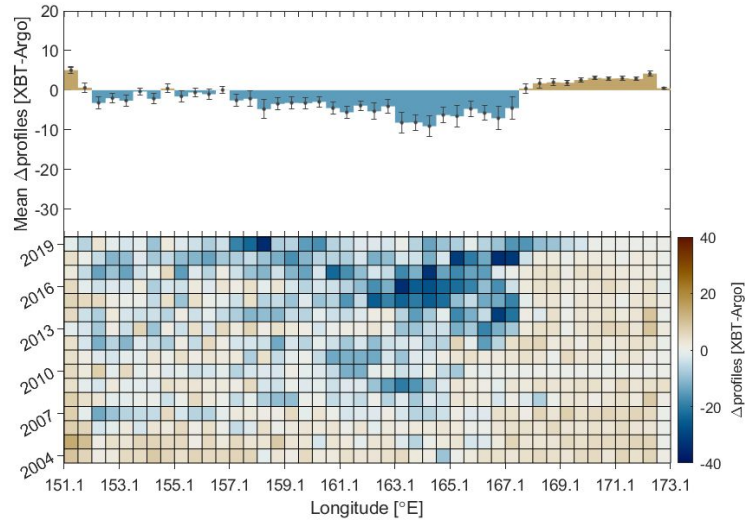
A1. PX06
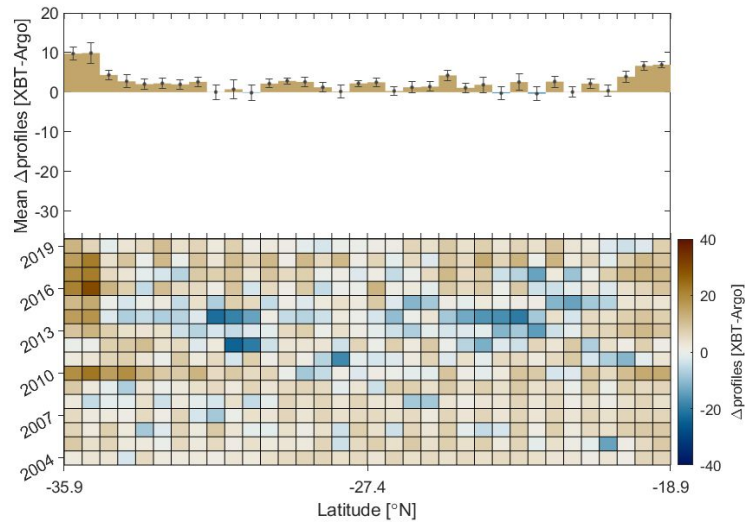
Figure A2: Difference in the number of HR-XBT and Argo profiles around the PX06 nominal transect for 2004-2019 in each 0.5°×3° orthogonal bin. Positive values (brown colours) indicate more HR-XBT profiles than Argo profiles. The histograms give the 2004-2019 yearly-averaged difference in the number of profiles, and the heatmaps give the difference in the number of profiles for each individual year. Error bars on the histograms represent ±1 standard error.
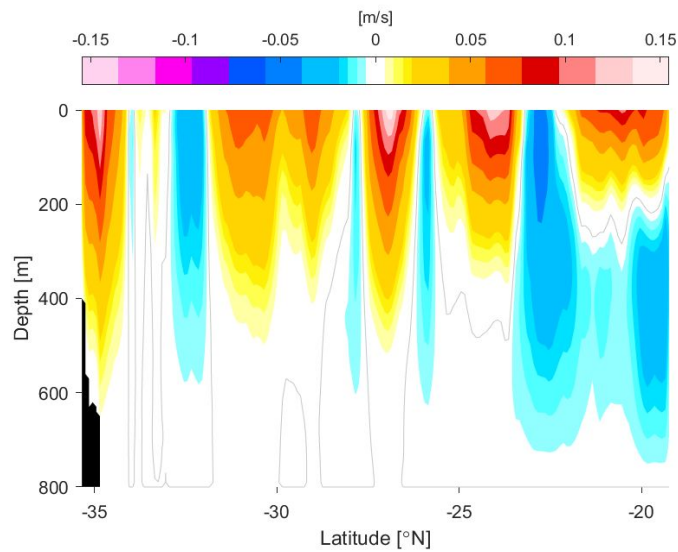
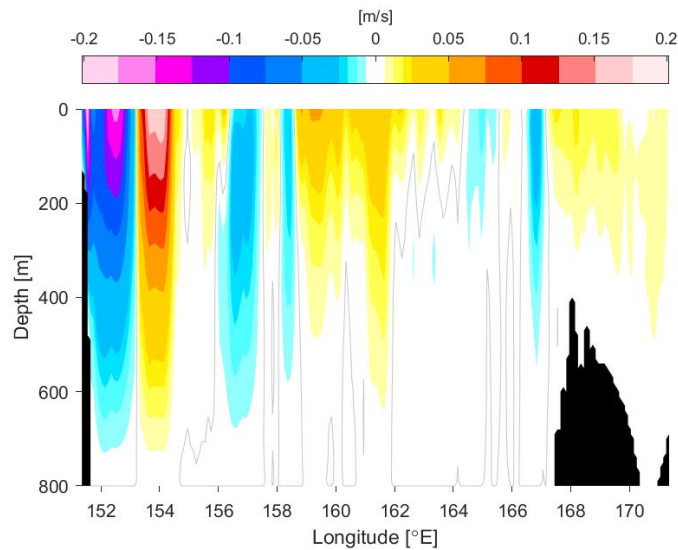

Figure A3: Geostrophic velocity relative to 800 m normal to the PX06 nominal transect for the Argo 2004-2018 mean climatology. Positive [negative] velocities are eastward [westward] and the zero velocity contour is indicated in grey.
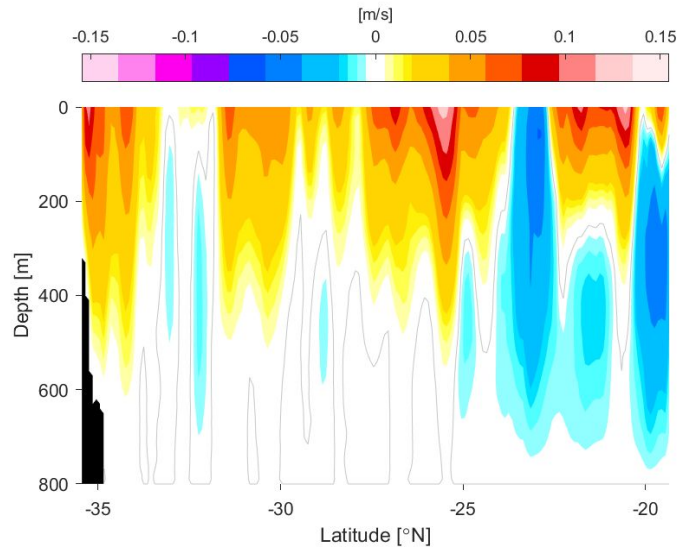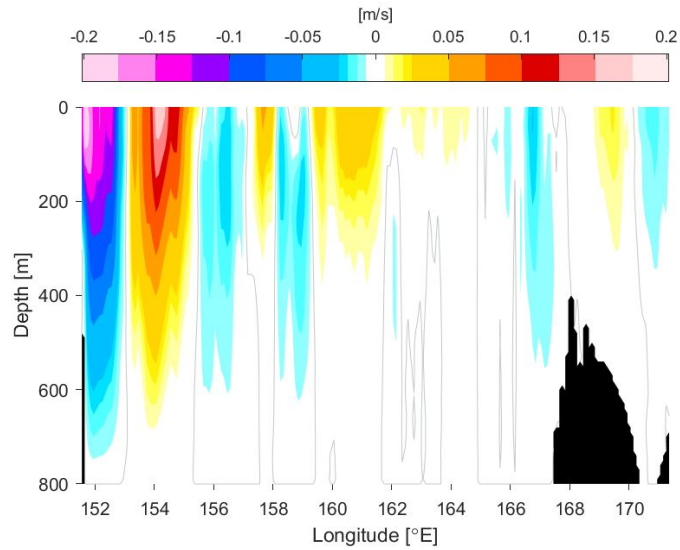
Figure A4: Geostrophic velocity relative to 800 m normal to the PX06 nominal transect for HR-XBT+Argo averaged between 2004-2019. Positive [negative] velocities are eastward [westward] and the zero velocity contour is indicated in grey.
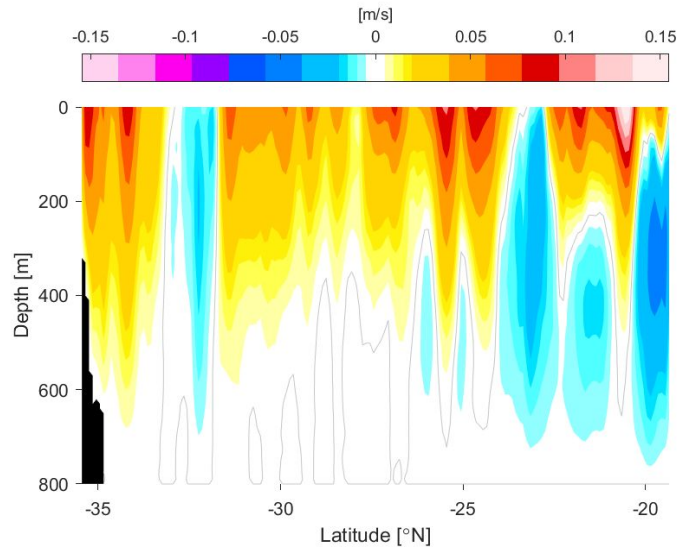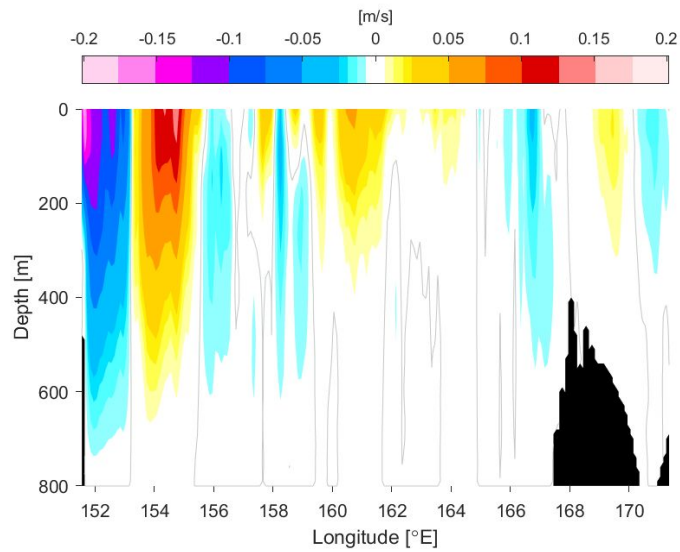

Figure A5: Geostrophic velocity relative to 800 m normal to the PX06 nominal transect for HR-XBT+Argo+Altimetry averaged between 2004-September 2019. Positive [negative] velocities are eastward [westward] and the zero velocity contour is indicated in grey.

27
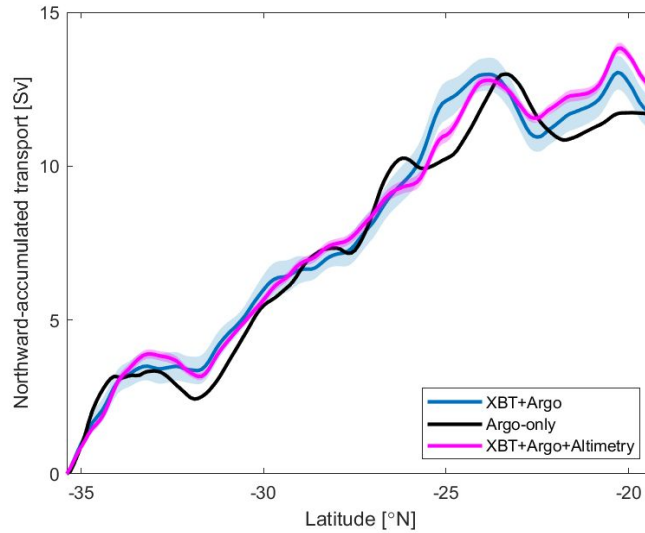
Figure A6: Mean northward-accumulated geostrophic transport (Sv) relative to 800 m normal to the PX06 nominal transect for HR-XBT+Argo (2004-2019 mean, blue), HR-XBT+Argo+Altimetry (2004-September 2019 mean, pink), and Argo-only (2004-2018 mean, black). The shading indicates ±1 standard error. Positive [negative] transports are eastward [westward].
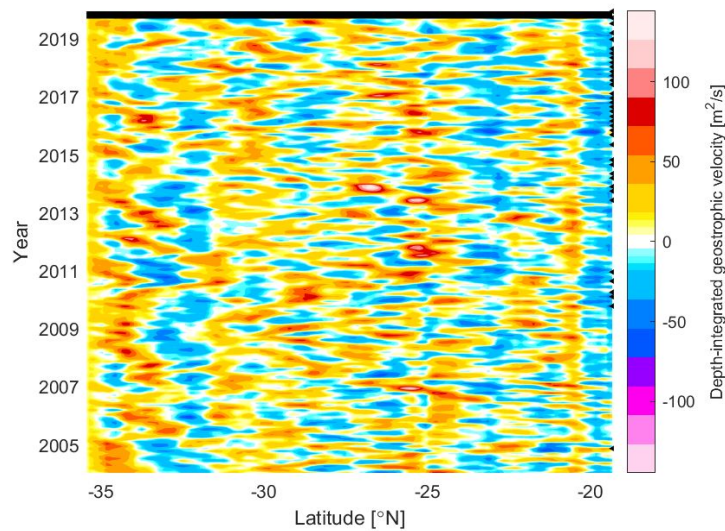
Figure A7: Monthly depth-integrated (0-800 m) geostrophic velocity (m^2 s^{-1}) normal to PX06 from HR-XBT+Argo+Altimetry. Positive [negative] velocities are eastward [westward]. The black arrows on the right indicate the times of the HR-XBT transects.

A2. PX30
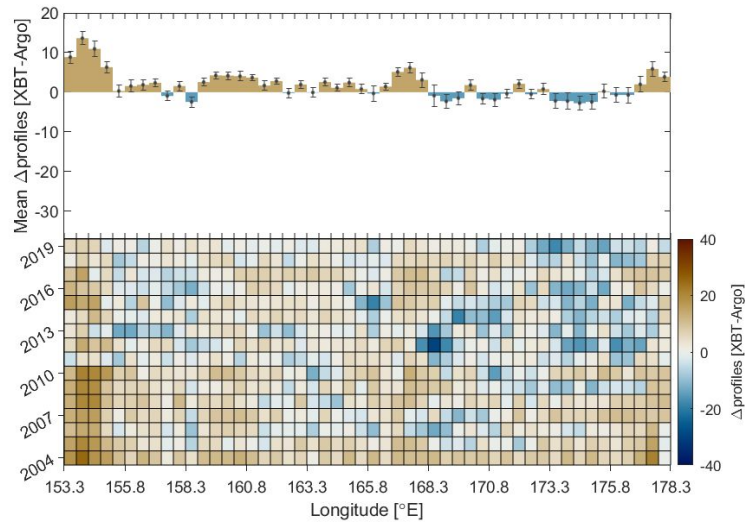
Figure A8: Difference in the number of HR-XBT and Argo profiles around the PX30 nominal transect for 2004-2019 in each 0.5°×3° orthogonal bin. Positive values (brown colours) indicate more HR-XBT profiles than Argo profiles. The histograms give the 2004-2019 yearly-averaged difference in the number of profiles, and the heatmaps give the difference in the number of profiles for each individual year. Error bars on the histograms represent ±1 standard error.
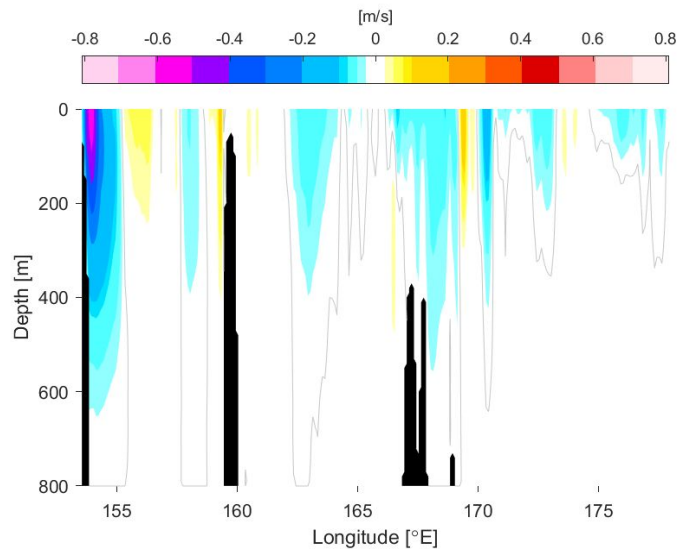
Figure A9: Geostrophic velocity relative to 800 m normal to the PX30 nominal transect for the Argo 2004-2018 mean climatology. Negative [positive] velocities are southward [northward] and the zero velocity contour is indicated in grey.
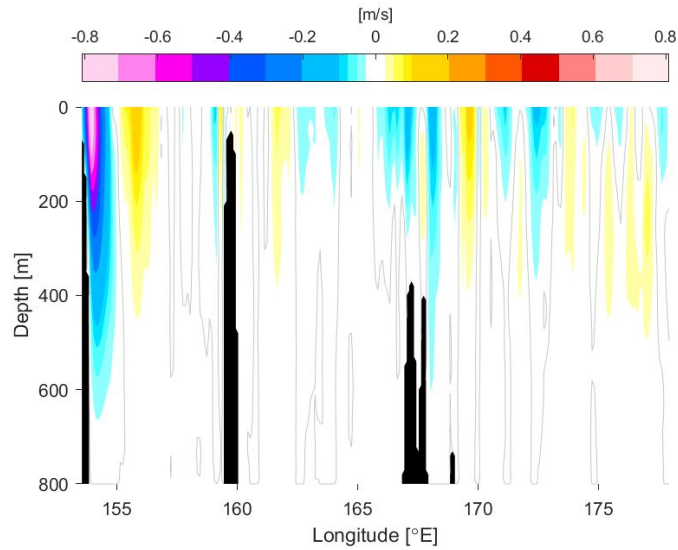
Figure A10: Geostrophic velocity relative to 800 m normal to the PX30 nominal transect for HR-XBT+Argo averaged between 2004-2019. Negative [positive] velocities are southward [northward] and the zero velocity contour is indicated in grey.
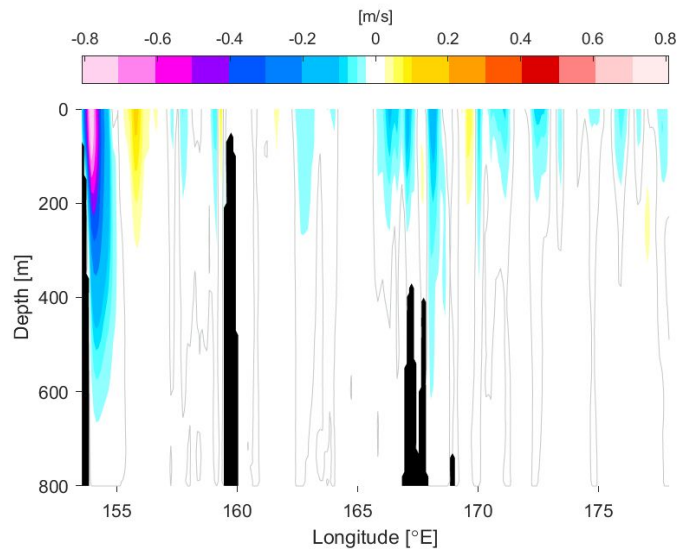
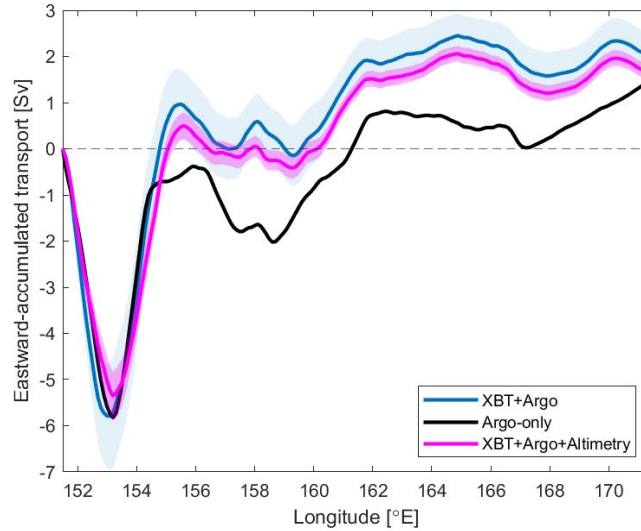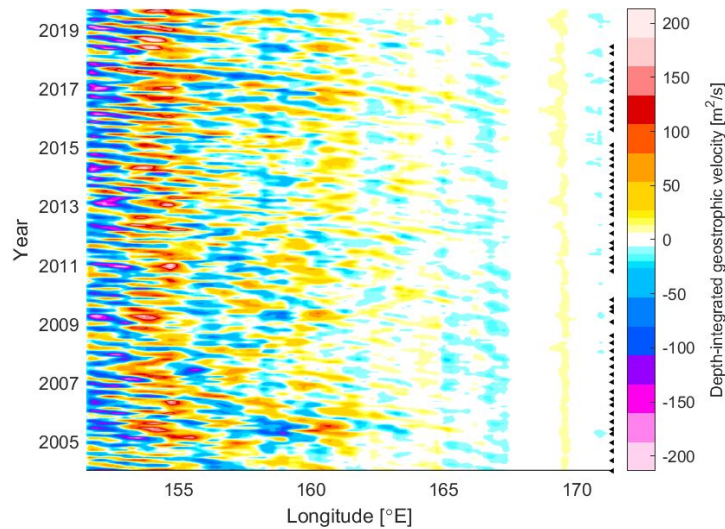**Figure A11:** Geostrophic velocity relative to 800 m normal to the PX30 nominal transect for HR-XBT+Argo+Altimetry averaged between 2004-September 2019. Negative [positive] velocities are southward [northward] and the zero velocity contour is indicated in grey.
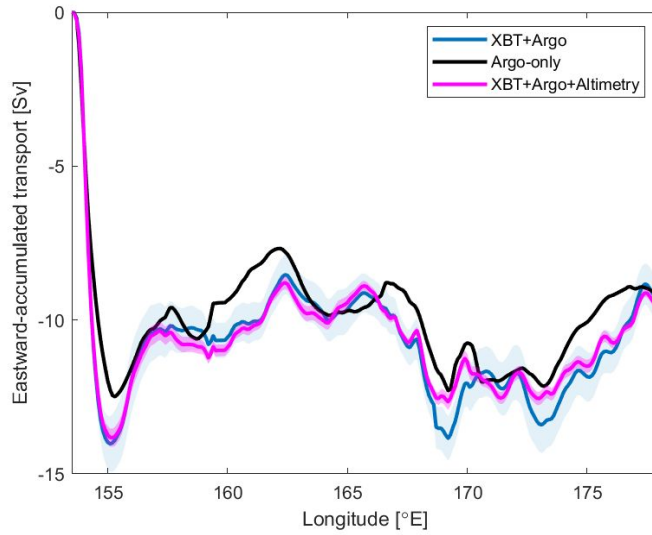
Figure A12: Mean eastward-accumulated geostrophic transport (Sv) relative to 800 m normal to the PX30 nominal transect for HR-XBT+Argo (2004-2019 mean, blue), HR-XBT+Argo+Altimetry (2004-September 2019 mean, pink), and Argo-only (2004-2018 mean, black). The shading indicates ±1 standard error. Negative [positive] transports are southward [northward].
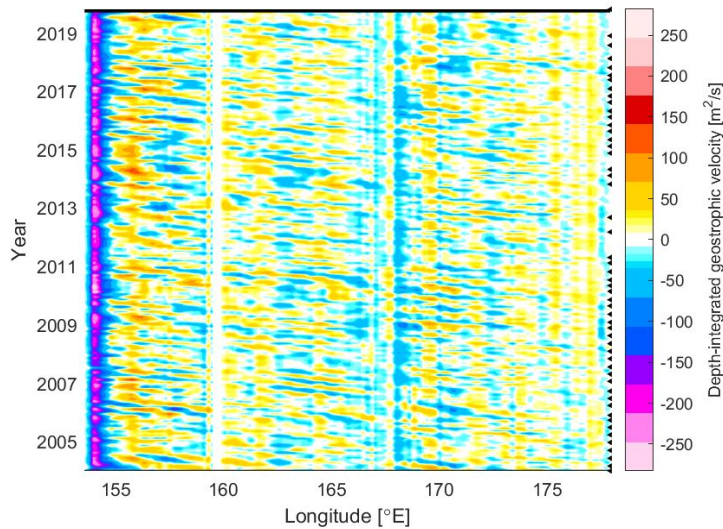
Figure A13: Monthly depth-integrated (0-800 m) geostrophic velocity (m^2 s^{-1}) normal to PX30 from HR-XBT+Argo+Altimetry. Negative [positive] velocities are southward [northward]. The black arrows on the right indicate the times of the HR-XBT transects.

31

A3. PX34

Figure A14: Difference in the number of HR-XBT and Argo profiles around the PX34 nominal transect for 2004-2019 in each 0.5°×3° orthogonal bin. Positive values (brown colours) indicate more HR-XBT profiles than Argo profiles. The histograms give the 2004-2019 yearly-averaged difference in the number of profiles, and the heatmaps give the difference in the number of profiles for each individual year. Error bars on the histograms represent ±1 standard error.
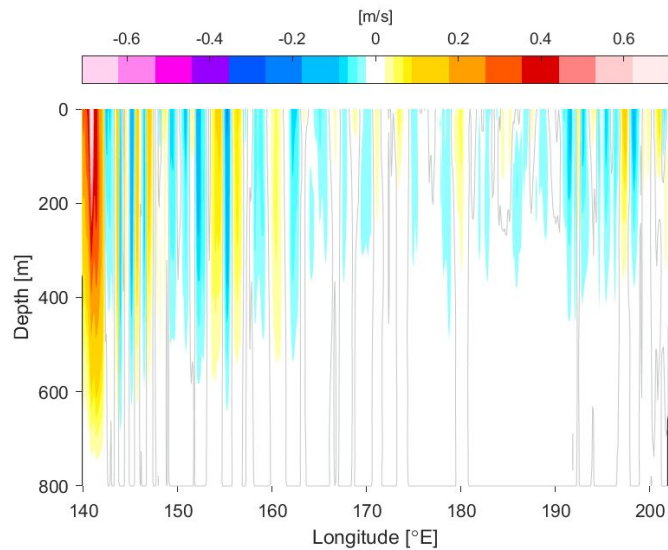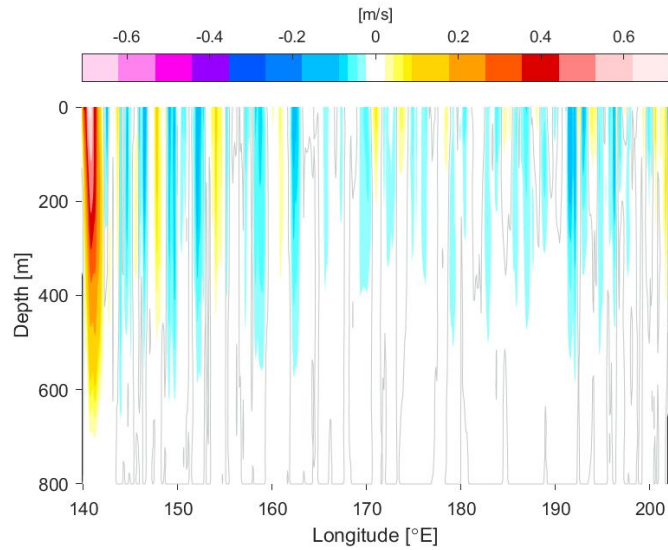

Figure A15: Geostrophic velocity relative to 800 m normal to the PX34 nominal transect for the Argo 2004-2018 mean climatology. Negative [positive] velocities are southward [northward] and the zero velocity contour is indicated in grey.

Figure A16: Geostrophic velocity relative to 800 m normal to the PX34 nominal transect for HR-XBT+Argo averaged between 2004-2019. Negative [positive] velocities are southward [northward] and the zero velocity contour is indicated in grey.
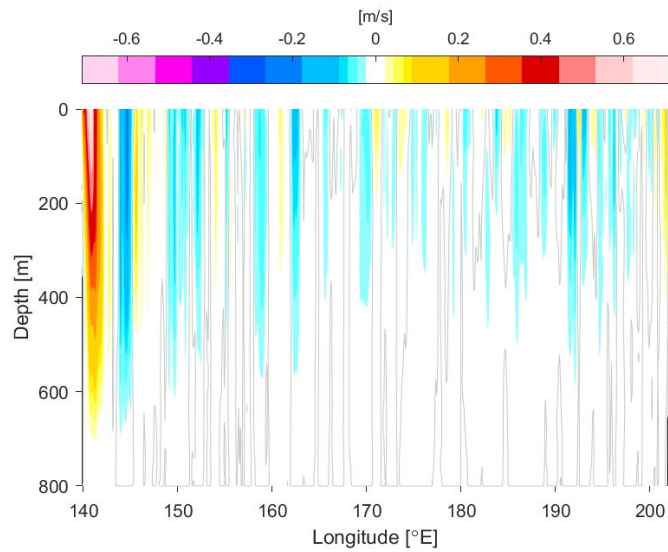

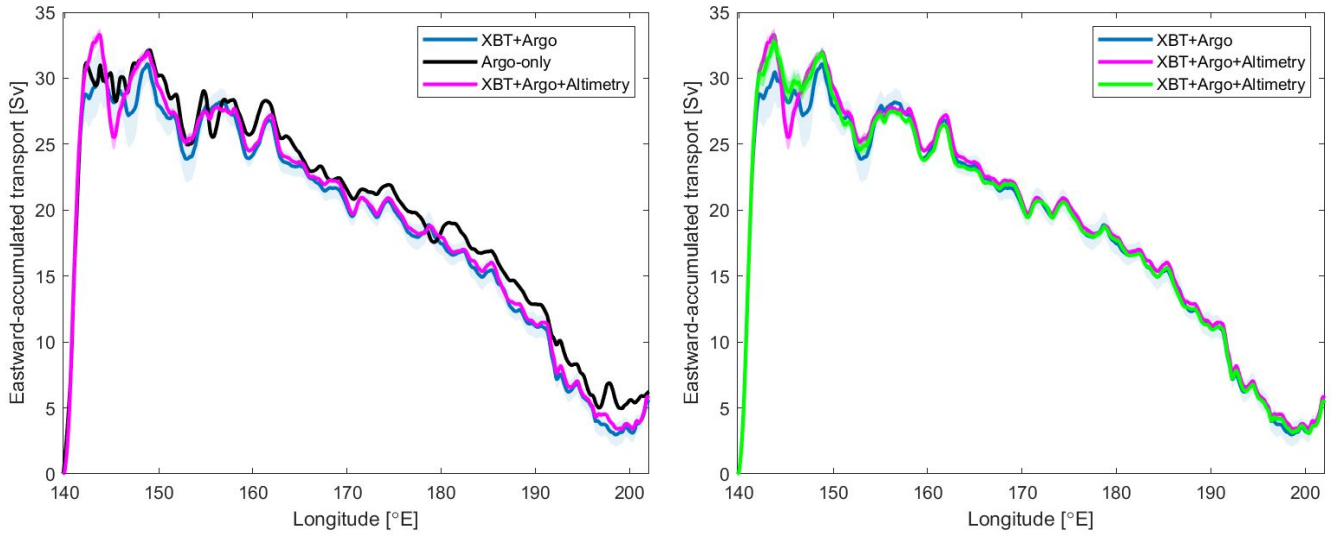**Figure A17:** Geostrophic velocity relative to 800 m normal to the PX34 nominal transect for HR-XBT+Argo+Altimetry averaged between 2004-September 2019. Negative [positive] velocities are southward [northward] and the zero velocity contour is indicated in grey.

Figure A18: Mean eastward-accumulated geostrophic transport (Sv) relative to 800 m normal to the PX34 nominal transect for HR-XBT+Argo (2004-2019 mean, blue), HR-XBT+Argo+Altimetry (2004-September 2019 mean, pink), and Argo-only (2004-2018 mean, black). The shading indicates ±1 standard error. Negative [positive] transports are southward [northward].
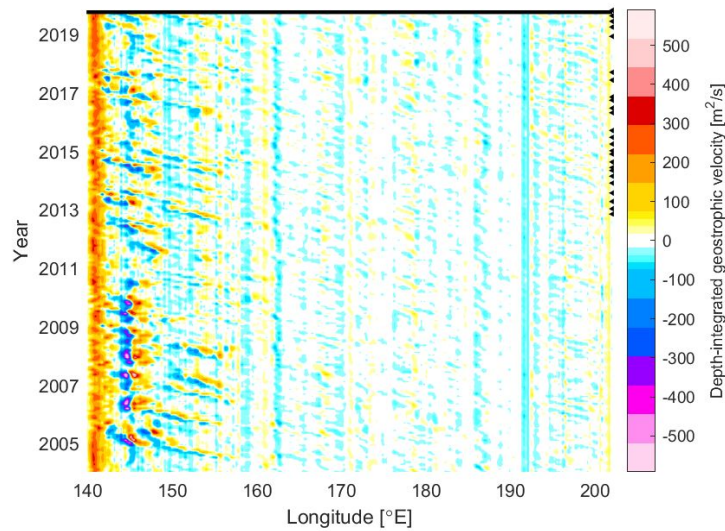

Figure A19: Monthly depth-integrated (0-800 m) geostrophic velocity (m^2 s^{-1}) normal to PX34 from HR-XBT+Argo+Altimetry. Negative [positive] velocities are southward [northward]. The black arrows on the right indicate the times of the HR-XBT transects.
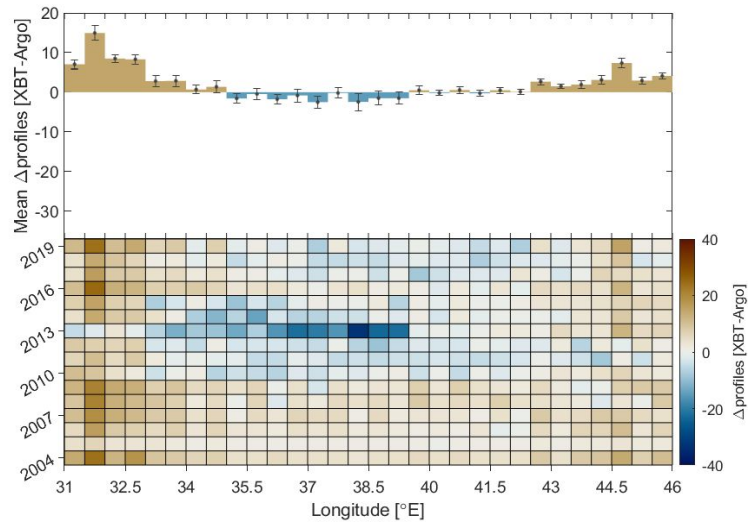
34

A4. PX40
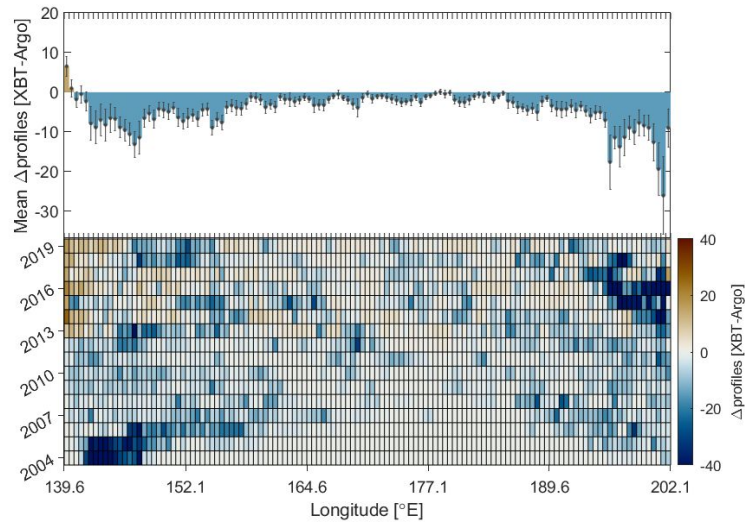
Figure A20: Difference in the number of HR-XBT and Argo profiles around the PX40 nominal transect for 2004-2019 in each 0.5°×3° orthogonal bin (note that HR-XBT profiling along the transect began in 2012). Positive values (brown colours) indicate more HR-XBT profiles than Argo profiles. The histograms give the 2004-2019 yearly-averaged difference in the number of profiles, and the heatmaps give the difference in the number of profiles for each individual year. Error bars on the histograms represent ±1 standard error.
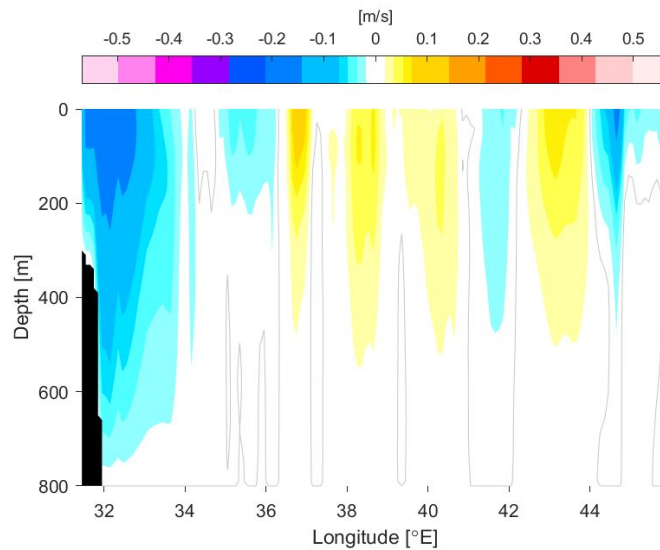

Figure A21: Geostrophic velocity relative to 800 m normal to the PX40 nominal transect for the Argo 2004-2018 mean climatology. Negative [positive] velocities are southward [northward] and the zero velocity contour is indicated in grey.
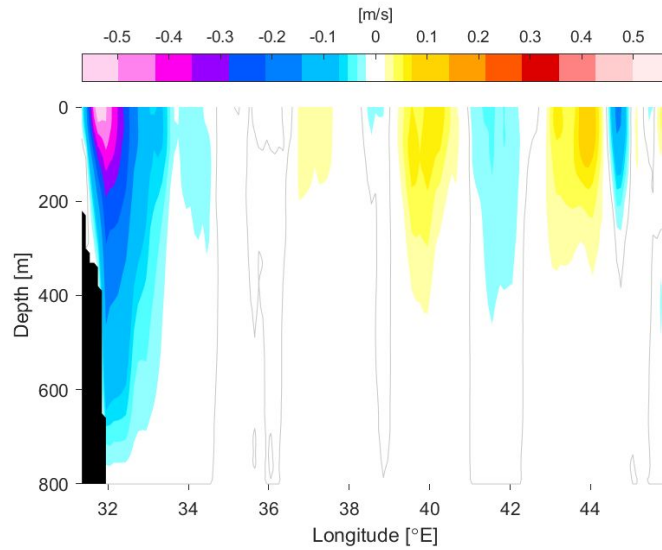
Figure A22: Geostrophic velocity relative to 800 m normal to the PX40 nominal transect for HR-XBT+Argo averaged between November 2012-2019. Negative [positive] velocities are southward [northward] and the zero velocity contour is indicated in grey.
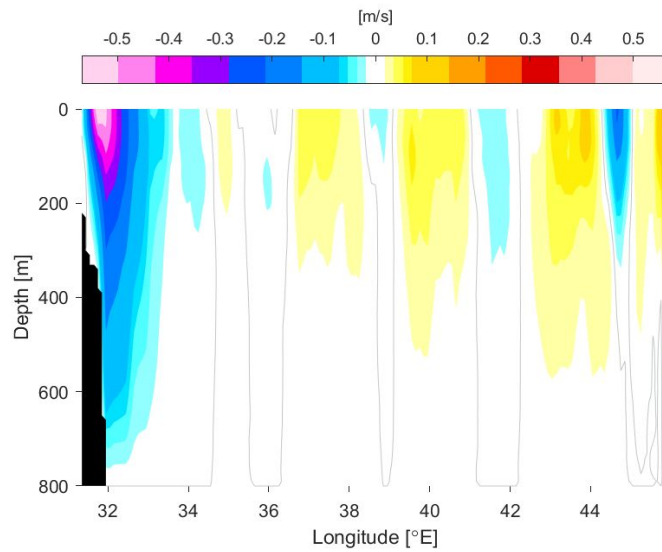

Figure A23: Geostrophic velocity relative to 800 m normal to the PX40 nominal transect for HR-XBT+Argo+Altimetry averaged between 2004-September 2019. Negative [positive] velocities are southward [northward] and the zero velocity contour is indicated in grey.
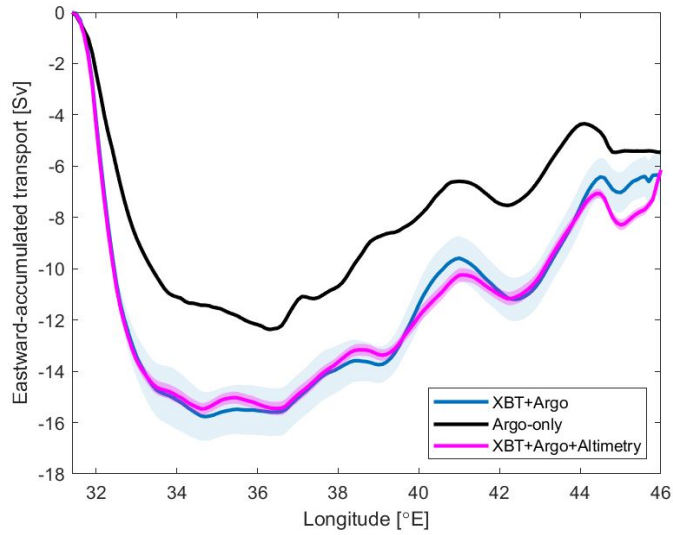
Figure A24: Mean eastward-accumulated geostrophic transport (Sv) relative to 800 m normal to the PX40 nominal transect for HR-XBT+Argo (November 2012-2019 mean, blue, both panels), HR-XBT+Argo+Altimetry (2004-September 2019 mean, pink, both panels), HR-XBT+Argo+Altimetry (November 2012-September 2019 mean, green, right panel), and Argo-only (2004-2018 mean, black, left panel). The shading indicates ±1 standard error. Negative [positive] transports are southward [northward].
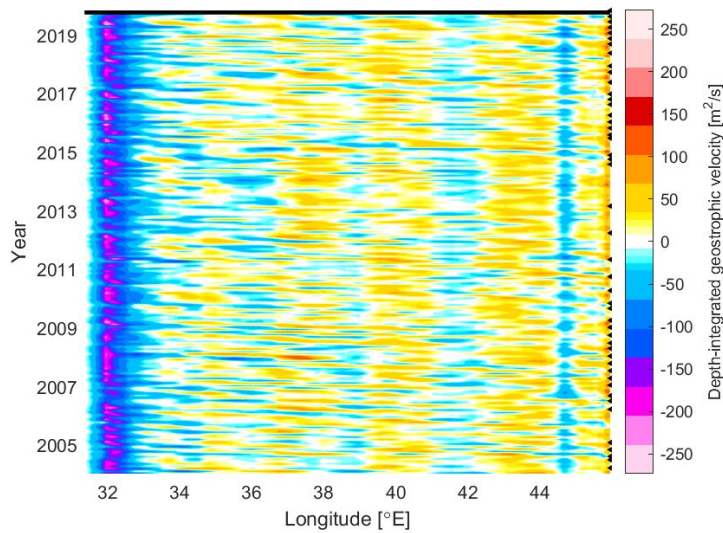

Figure A25: Monthly depth-integrated (0-800 m) geostrophic velocity (m^2 s^{-1}) normal to PX40 from HR-XBT+Argo+Altimetry. Negative [positive] velocities are southward [northward]. The black arrows on the right indicate the times of the HR-XBT transects.
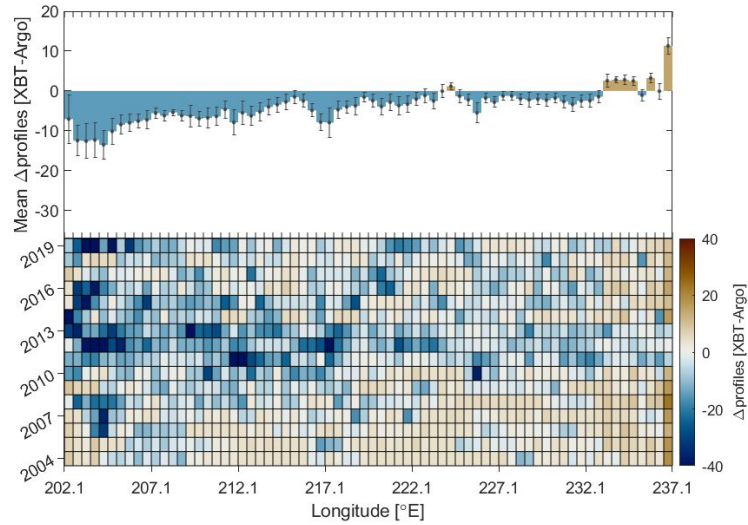
37

A5. IX21

Figure A26: Difference in the number of HR-XBT and Argo profiles around the IX21 nominal transect for 2004-2019 in each 0.5°×3° orthogonal bin. Positive values (brown colours) indicate more HR-XBT profiles than Argo profiles. The histograms give the 2004-2019 yearly-averaged difference in the number of profiles, and the heatmaps give the difference in the number of profiles for each individual year. Error bars on the histograms represent ±1 standard error.
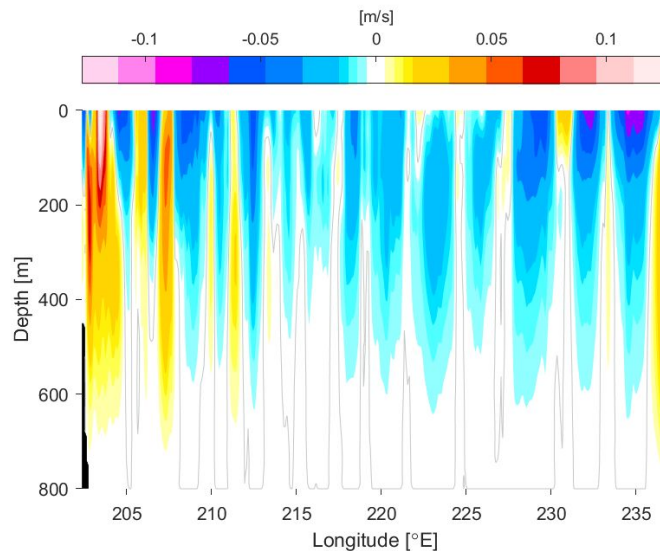

Figure A27: Geostrophic velocity relative to 800 m normal to the IX21 nominal transect for the Argo 2004-2018 mean climatology. Negative [positive] velocities are southward [northward] and the zero velocity contour is indicated in grey.
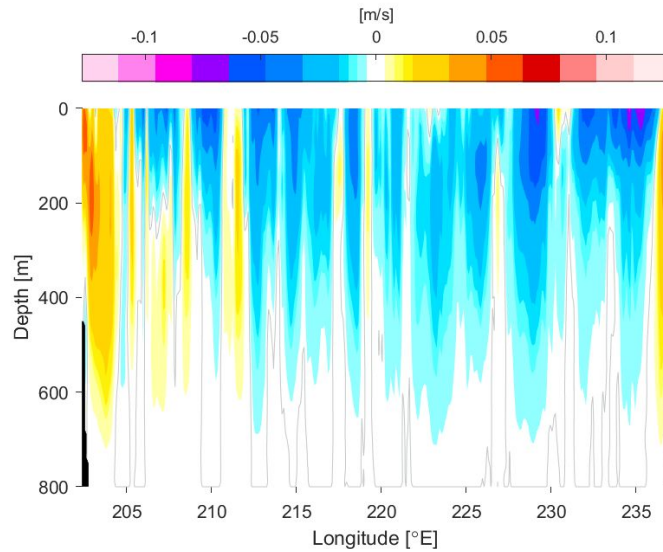
38

Figure A28: Geostrophic velocity relative to 800 m normal to the IX21 nominal transect for HR-XBT+Argo averaged between 2004-2019. Negative [positive] velocities are southward [northward] and the zero velocity contour is indicated in grey.
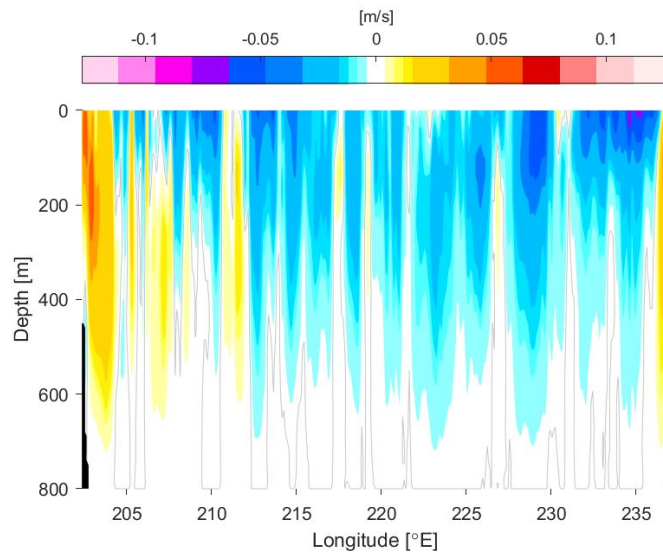

Figure A29: Geostrophic velocity relative to 800 m normal to the IX21 nominal transect for HR-XBT+Argo+Altimetry averaged between 2004-September 2019. Negative [positive] velocities are southward [northward] and the zero velocity contour is indicated in grey.
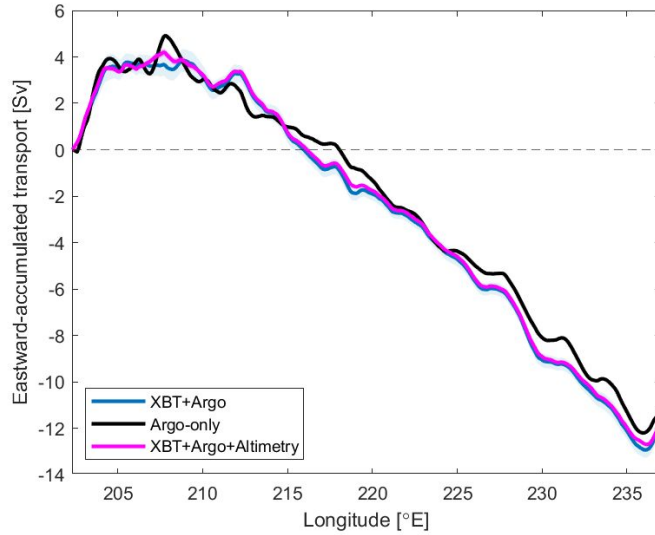
Figure A30: Mean eastward-accumulated geostrophic transport (Sv) relative to 800 m normal to the IX21 nominal transect for HR-XBT+Argo (2004-2019 mean, blue), HR-XBT+Argo+Altimetry (2004-September 2019 mean, pink), and Argo-only (2004-2018 mean, black). The shading indicates ±1 standard error. Negative [positive] transports are southward [northward].

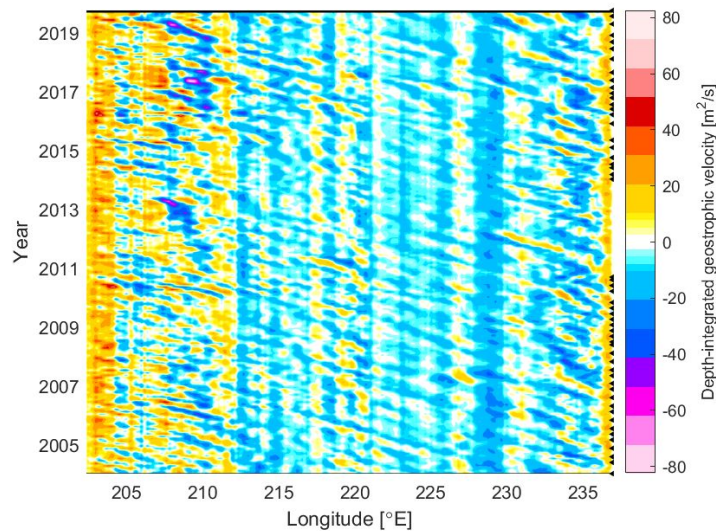**Figure A31:** Monthly depth-integrated (0-800 m) geostrophic velocity (m^2 s^{-1}) normal to IX21 from HR-XBT+Argo+Altimetry. Negative [positive] velocities are southward [northward]. The black arrows on the right indicate the times of the HR-XBT transects.

A6. PX37

Figure A32: Difference in the number of HR-XBT and Argo profiles around the PX37 nominal transect for 2004-2019 in each 0.5°×3° orthogonal bin. Positive values (brown colours) indicate more HR-XBT profiles than Argo profiles. The histograms give the 2004-2019 yearly-averaged difference in the number of profiles, and the heatmaps give the difference in the number of profiles for each individual year. Error bars on the histograms represent ±1 standard error.

Figure A33: Geostrophic velocity relative to 800 m normal to the PX37 nominal transect for the Argo 2004-2018 mean climatology. Negative [positive] velocities are southward [northward] and the zero velocity contour is indicated in grey.

Figure A34: Geostrophic velocity relative to 800 m normal to the PX37 nominal transect for HR-XBT+Argo averaged between 2004-2019. Negative [positive] velocities are southward [northward] and the zero velocity contour is indicated in grey.

Figure A35: Geostrophic velocity relative to 800 m normal to the PX37 nominal transect for HR-XBT+Argo+Altimetry averaged between 2004-September 2019. Negative [positive] velocities are southward [northward] and the zero velocity contour is indicated in grey.

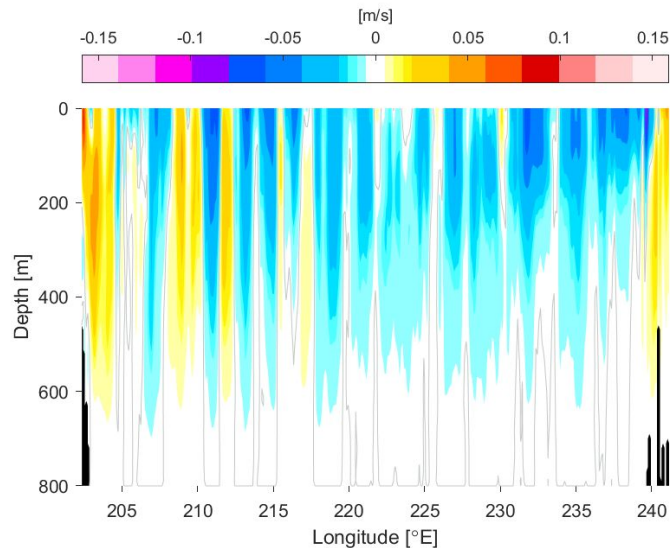**Figure A36:** Mean eastward-accumulated geostrophic transport (Sv) relative to 800 m normal to the PX37 nominal transect for HR-XBT+Argo (2004-2019 mean, blue), HR-XBT+Argo+Altimetry (2004-September 2019 mean, pink), and Argo-only (2004-2018 mean, black). The shading indicates ±1 standard error. Negative [positive] transports are southward [northward].

Figure A37: Monthly depth-integrated (0-800 m) geostrophic velocity (m^2 s^{-1}) normal to PX37 from HR-XBT+Argo+Altimetry. Negative [positive] velocities are southward [northward]. The black arrows on the right indicate the times of the HR-XBT transects.

A7. PX37S
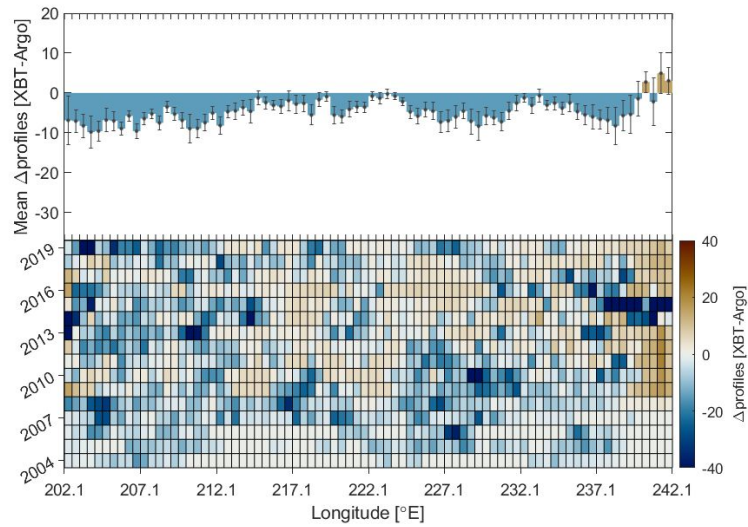
Figure A38: Difference in the number of HR-XBT and Argo profiles around the PX37S nominal transect for 2004-2019 in each 0.5°×3° orthogonal bin (note that HR-XBT profiling along the transect began in 2008). Positive values (brown colours) indicate more HR-XBT profiles than Argo profiles. The histograms give the 2004-2019 yearly-averaged difference in the number of profiles, and the heatmaps give the difference in the number of profiles for each individual year. Error bars on the histograms represent ±1 standard error.
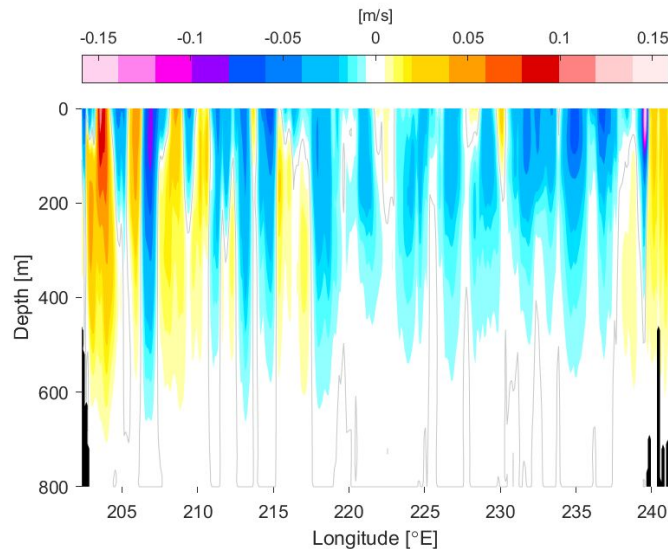
Figure A39: Geostrophic velocity relative to 800 m normal to the PX37S nominal transect for the Argo 2004-2018 mean climatology. Negative [positive] velocities are southward [northward] and the zero velocity contour is indicated in grey.

Figure A40: Geostrophic velocity relative to 800 m normal to the PX37S nominal transect for HR-XBT+Argo averaged between November 2008-2019. Negative [positive] velocities are southward [northward] and the zero velocity contour is indicated in grey.
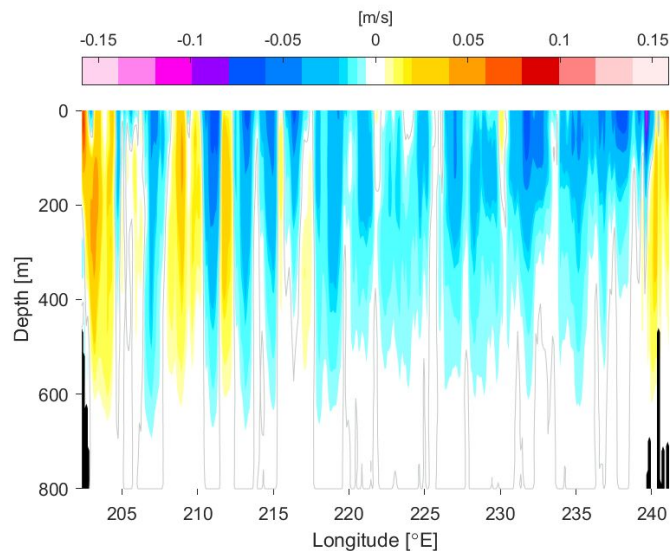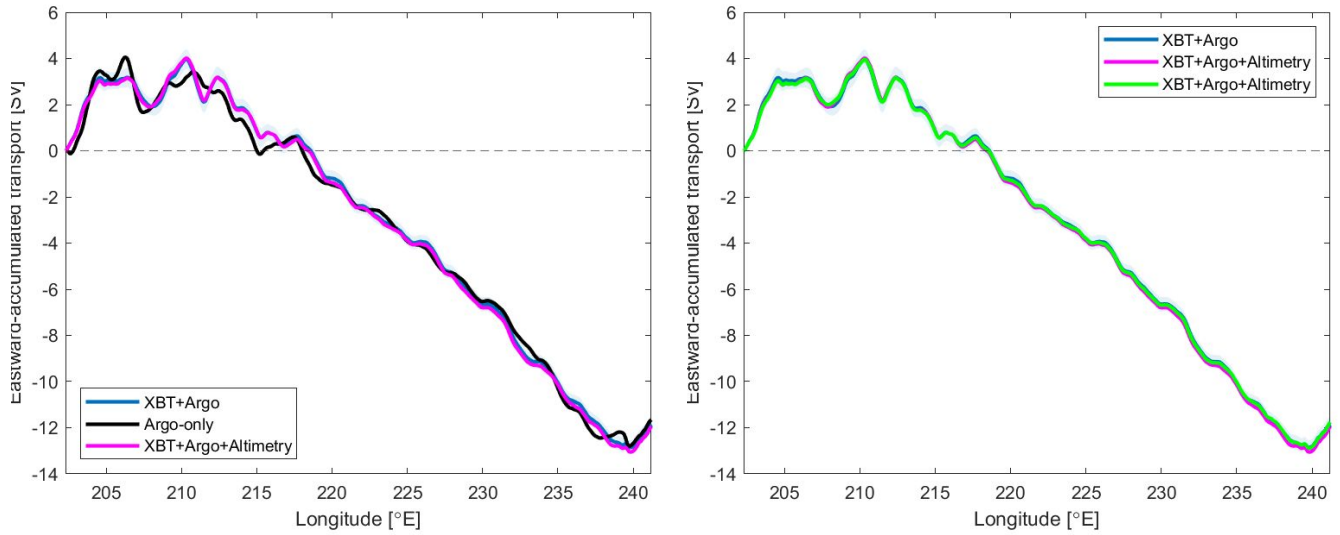

Figure A41: Geostrophic velocity relative to 800 m normal to the PX37S nominal transect for HR-XBT+Argo+Altimetry averaged between 2004-September 2019. Negative [positive] velocities are southward [northward] and the zero velocity contour is indicated in grey.

45

Figure A42: Mean eastward-accumulated geostrophic transport (Sv) relative to 800 m normal to the PX37S nominal transect for HR-XBT+Argo (November 2008-2019 mean, blue, both panels), HR-XBT+Argo+Altimetry (2004-September 2019 mean, pink, both panels), HR-XBT+Argo+Altimetry (November 2008-September 2019 mean, green, right panel), and Argo-only (2004-2018 mean, black, left panel). The shading indicates ±1 standard error. Negative [positive] transports are southward [northward].
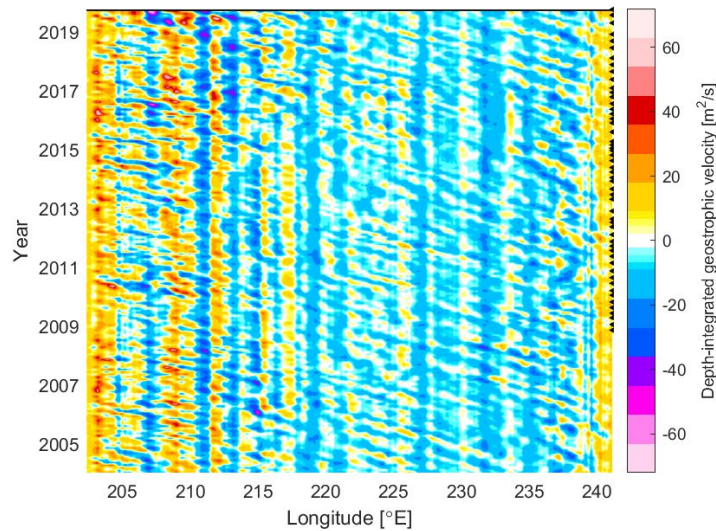

Figure A43: Monthly depth-integrated (0-800 m) geostrophic velocity (m^2 s^{-1}) normal to PX37S from HR-XBT+Argo+Altimetry. Negative [positive] velocities are southward [northward]. The black arrows on the right indicate the times of the HR-XBT transects.
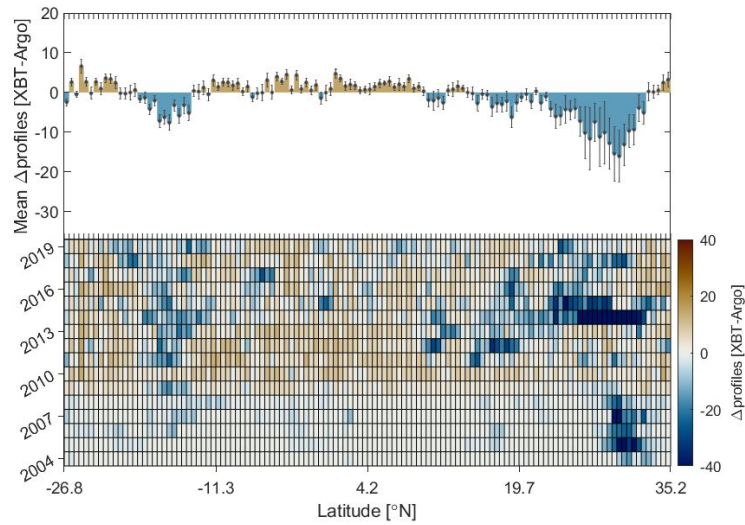
A8. PX05

Figure A44: Difference in the number of HR-XBT and Argo profiles around the PX05 nominal transect for 2004-2019 in each 0.5°×3° orthogonal bin (note that HR-XBT profiling along the transect began in 2009). Positive values (brown colours) indicate more HR-XBT profiles than Argo profiles. The histograms give the 2004-2019 yearly-averaged difference in the number of profiles, and the heatmaps give the difference in the number of profiles for each individual year. Error bars on the histograms represent ±1 standard error.
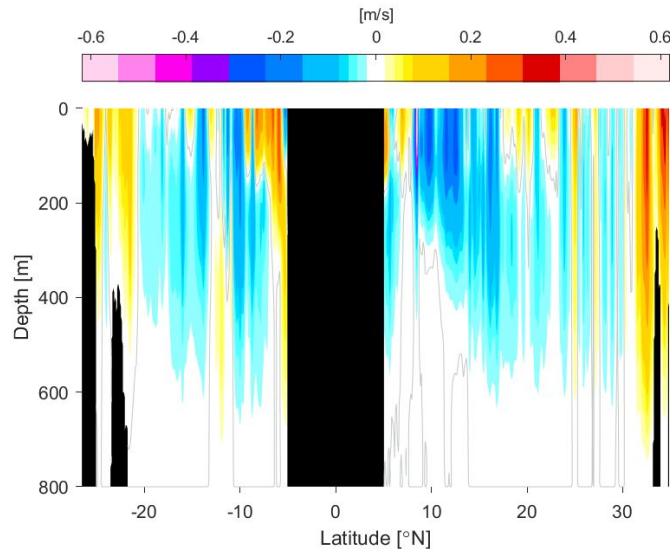

Figure A45: Geostrophic velocity relative to 800 m normal to the PX05 nominal transect for the Argo 2004-2018 mean climatology. Negative [positive] velocities are eastward [westward] and the zero velocity contour is indicated in grey. Velocities within ±5° of the equator are excluded.
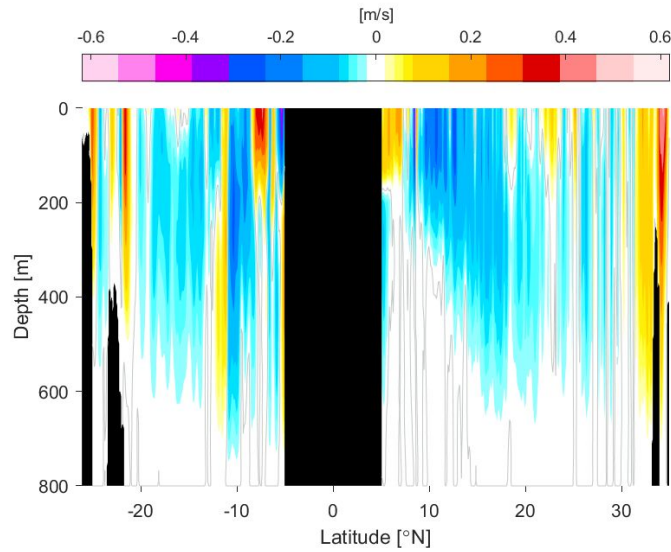
Figure A46: Geostrophic velocity relative to 800 m normal to the PX05 nominal transect for HR-XBT+Argo averaged between August 2009-2019. Negative [positive] velocities are eastward [westward] and the zero velocity contour is indicated in grey. Velocities within ±5° of the equator are excluded.
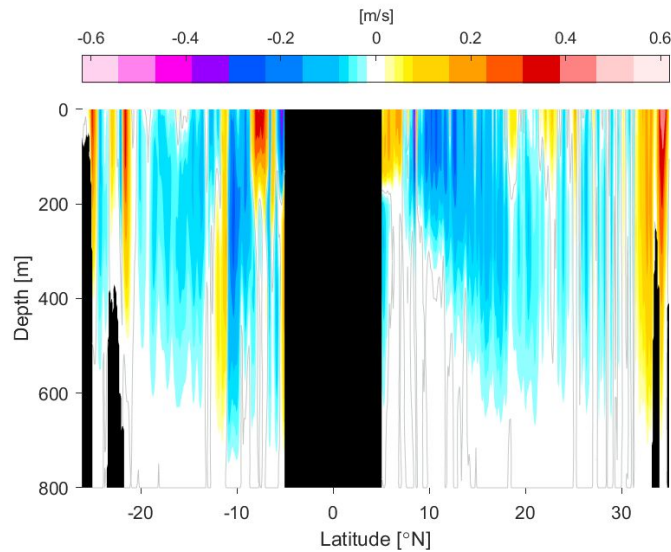

Figure A47: Geostrophic velocity relative to 800 m normal to the PX05 nominal transect for HR-XBT+Argo+Altimetry averaged between 2004-September 2019. Negative [positive] velocities are eastward [westward] and the zero velocity contour is indicated in grey. Velocities within ±5° of the equator are excluded.
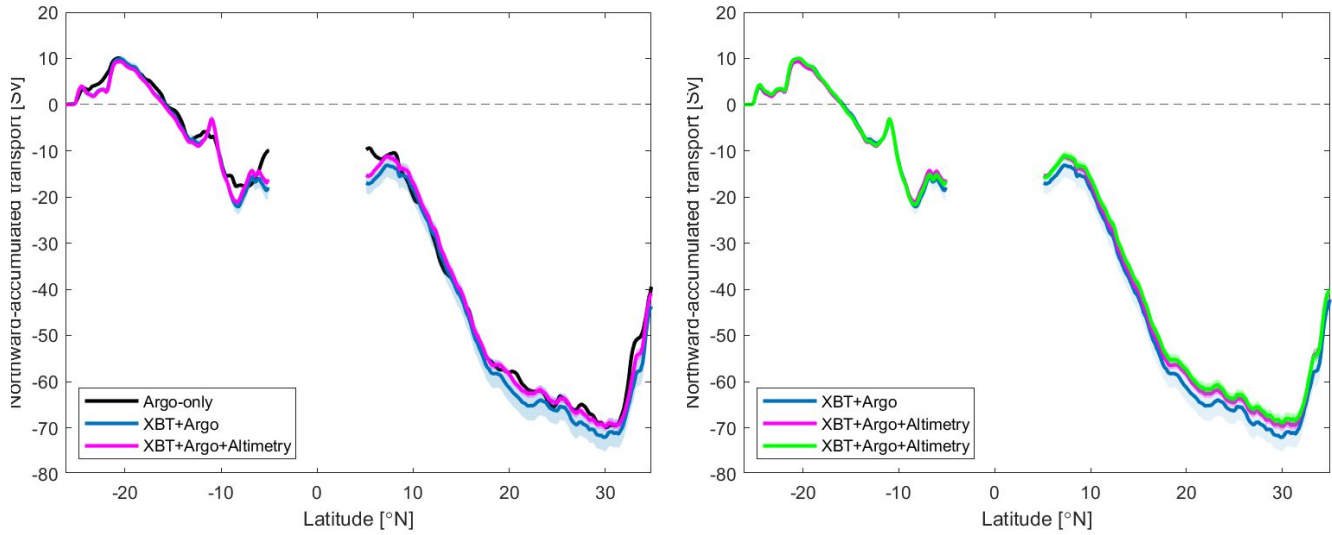
Figure A48: Mean northward-accumulated geostrophic transport (Sv) relative to 800 m normal to the PX05 nominal transect for HR-XBT+Argo (August 2009-2019 mean, blue, both panels), HR-XBT+Argo+Altimetry (2004-September 2019 mean, pink, both panels), HR-XBT+Argo+Altimetry (August 2009-September 2019 mean, green, right panel), and Argo-only (2004-2018 mean, black, left panel). The shading indicates ±1 standard error. Negative [positive] transports are eastward [westward]. Transports within ±5° of the equator are excluded.
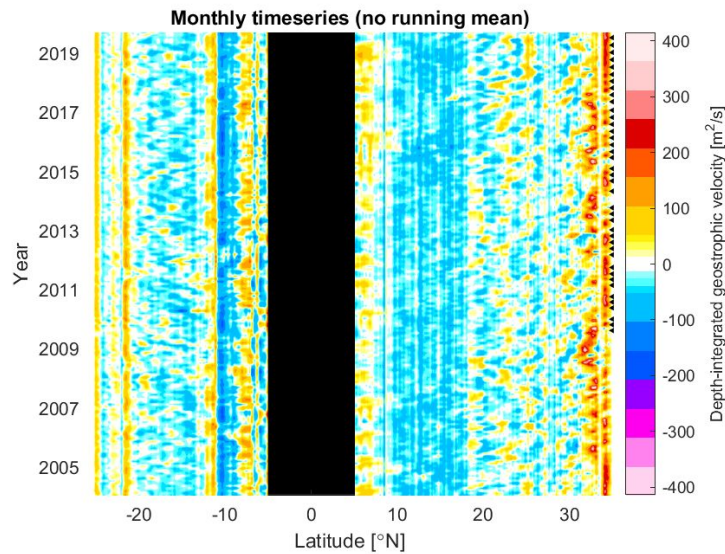

Figure A49: Monthly depth-integrated (0-800 m) geostrophic velocity (m^2 s^{-1}) normal to PX05 from HR-XBT+Argo+Altimetry. Negative [positive] velocities are eastward [westward]. The black arrows on the right indicate the times of the HR-XBT transects. Depth-integrated velocities within ±5° of the equator are excluded.

49